



UNIVERSIDADE FEDERAL DE PERNAMBUCO
CENTRO DE CIÊNCIAS EXATAS E DA NATUREZA
PROGRAMA DE PÓS-GRADUAÇÃO EM FÍSICA

JEAN FELIPE OLIVEIRA DA SILVA

Ferromagnetic Resonance by micromagnetic simulation in hollow pillars

Recife

2022

JEAN FELIPE OLIVEIRA DA SILVA

Ferromagnetic Resonance by micromagnetic simulation in hollow pillars

Dissertação apresentada ao Programa de Pós-graduação em Física do Centro de Ciências Exatas e da Natureza da Universidade Federal de Pernambuco, como parte dos requisitos necessários para obtenção do título de Mestre em Física.

Área de Concentração: Física da Matéria Condensada

Orientador: Prof. Dr. Eduardo Padrón Hernández

Recife

2022

Catálogo na fonte
Bibliotecária Nataly Soares Leite Moro, CRB4-1722

S586f Silva, Jean Felipe Oliveira da
Ferromagnetic Resonance by micromagnetic simulation in hollow pillars /
Jean Felipe Oliveira da Silva. – 2022.
76 f.: il., fig., tab.

Orientador: Eduardo Padrón Hernández.
Dissertação (Mestrado) – Universidade Federal de Pernambuco. CCEN,
Física, Recife, 2022.
Inclui referências e anexo.

1. Física da matéria condensada. 2. Ressonância ferromagnética. 3.
Simulação ferromagnética. 4. Ferromagnetismo. 5. Campo de anisotropia I.
Padrón Hernández, Eduardo (orientador). II. Título.

530.41 CDD (23. ed.) UFPE- CCEN 2022 - 28

JEAN FELIPE OLIVEIRA DA SILVA

**FERROMAGNETIC RESONANCE BY MICROMAGNETIC
SIMULATION IN HOLLOW PILLARS**

Dissertação apresentada ao Programa de Pós-Graduação em Física da Universidade Federal de Pernambuco, como requisito parcial para a obtenção do título de Mestre em Física.

Aprovada em: 22/02/2022.

BANCA EXAMINADORA

Prof. Eduardo Padrón Hernández
Orientador
Universidade Federal de Pernambuco

Prof. Renê Rodrigues Montenegro Filho
Examinador Interno
Universidade Federal de Pernambuco

Prof. Roberto Lázaro Rodríguez Suárez
Examinador Externo
Pontificia Universidad Católica de Chile

Dedico esta dissertação a minha avó, que me inspira todos os dias. Este trabalho mostra que todo seu investimento e dedicação valeram a pena.

ACKNOWLEDGEMENTS

Agradeço primeiramente ao meu Orientador, o Professor Eduardo Padrón que me levou de um estudante frustrado a um pesquisador com sua paciência e filosofia de vida. Agradeço também a oportunidade de fazer parte de seu grupo de pesquisa, onde pude rever o Professor que me aliciou ao curso de Física durante meu Ensino Médio, Fred Revoredo. Além dele conheci outros amigos como (em ordem alfabética) Aldo, Carla, Daniel, Dyego, Filipe, Johanny, Jurandir, Lauretan, Matheus Fairbanks, Raquel, Raudel, Samuel, Von Ivson, Wemerson, William, Yuset...Dentre outros que não conheci... Também agradeço pela companhia e ajuda de amigos que fiz ao longo da graduação como Jefferson e Kacio, além dos já citados do laboratório. Agradeço também a Írio pelas dicas importantes para minha formação científica, assim como Matheus Valença.

Agradeço a pessoa que torna nossa casa um lar e que me ajuda a sorrir todos os dias com sua simpatia e resiliência, Anna Carolina. Você torna minha vida melhor com sua alegria e sempre me ajuda em diversas áreas da minha vida, eu amo você. Agradeço também pelo presente que recebi por ser pai de Alfa que também herdou as principais características de sua mãe. É ótimo poder contar com vocês em minha vida. Agradeço a Alfa, que um dia vai ler este texto, por todos os momentos divertidos que tivemos. Peço desculpa por nem sempre estar disponível nos momentos que você precisava. Você me trouxe muita felicidade em cada palavra aprendida e cada passo intelectual e físico dado. Ser o seu pai é um privilégio único. Agradeço também aos meus pais por sempre me incentivarem nos estudos e por sempre acreditarem em meu trabalho. Agradeço também por todo carinho e cuidado que minha Tia, Edinece, teve por mim ao longo dos anos, herdado por sua mãe Nice que foi mais uma pessoa maravilhosa que surgiu em minha vida. Agradeço a minha avó por sua existência e força, que me impulsiona em minha trajetória acadêmica. Sua vontade por aprender e conhecer me enchem de orgulho!

Agradecimentos especiais são direcionados ao projeto OOMMF do ITL/NIST¹ que foi o software utilizado nesta dissertação. A agência CNPq pelo apoio financeiro e as agências CAPES, FINEP e FACEPE que possibilitam a ciência acontecer neste país, mesmo com todas as adversidades. Por último agradeço ao Programa de Pós-Graduação em Física da UFPE por todo conhecimento e ajuda que a mim foram passados. Agradeço também a todos funcionários que fazem o Departamento de Física funcionar com excelência.

¹ <https://www.nist.gov/>

ABSTRACT

In this work, using computational simulation, unitary structures of nanopillars and nanopillar arrangements were analyzed. The study was carried out using The Object Oriented MicroMagnetic Framework The Object Oriented MicroMagnetic Framework (OOMMF) simulator using Finite Difference Method (FDM) to simulate Ferromagnetic Resonance (FMR) in the studied systems. The square nickel nanopillars have lateral length $D = 30$ nm and height $L = 120$ nm. The size of the internal cavity in this system was also varied, with values of $d = 0$ nm (solid pillar), $d = 10$ nm and $d = 20$ nm. To study the column arrangements, they were arranged in a 3×3 matrix. In addition to inheriting the cavity variation characteristics, each column had an initial distance of $a - D = 5$ nm between its neighbors. This distance was changed to $a - D = 10$ nm, $a - D = 20$ nm and $a - D = 50$ nm to analyze the influence on the dipole interactions of this system. The *Zeeman* interaction was considered when an external magnetic field was placed on the surface. Due to the geometry of this system, the anisotropy field H_A was studied for each nanopillar system. The theoretical model for adjusting our parameters and analyzing the anisotropy field was the Kittel equations. Main and secondary peak frequencies were studied for unitary columns to obtain information about the anisotropy field of the sample. For the primary peaks, compared with works in the literature, it was noticed that the ferromagnetic resonance response came from the sides of the structure on the z-axis, in the secondary peaks, the values of H_A for the perpendicular field have large divergences according to the model. It was also possible to observe that the adjustment for the anisotropy field improves the greater the value of d . Due to the analyzes made for unitary columns, the secondary peaks for column arrangements were not analyzed. For primary peaks with the applied perpendicular field, it was observed that the Kittel equation for FMR does not correctly adjust the values for H_A . In the analysis of parallel fields, we tried to analyze the influence of neighboring columns on the value of H_A . A model was used considering the system's packaging factor. In this model, it was compared when considering the cavity in the center of the columns and assuming them to be solid columns. From the comparison with results in the literature, the packing factor that best described the system was the first, as more dipole effects are added to the system.

Keywords: ferromagnetic resonance; ferromagnetic simulation; ferromagnetism; anisotropy field.

RESUMO

Neste trabalho foi analisado, por meio de simulação computacional, estruturas unitárias de nanopilar e arranjos de nanopilares. O estudo foi feito utilizando o simulador *OOMMF* utilizando o Método de Diferenças Finitas (MDF) para simular Ressonância Ferromagnética nos sistemas estudados. Os nanopilares quadrados de Níquel possuem comprimento lateral $D = 30$ nm e altura $L = 120$ nm. Também foi variado o tamanho da cavidade interna neste sistema, com valores de $d = 0$ nm (pilar sólido), $d = 10$ nm e $d = 20$ nm. Para o estudo dos arranjos de pilares, estes foram dispostos em uma matriz 3×3 . Além de herdar as características de variação da cavidade, cada pilar possuía uma distância inicial de $a - D = 5$ nm entre seus vizinhos. Esta distância foi alterada para $a - D = 10$ nm, $a - D = 20$ nm e $a - D = 50$ nm para analisar a influência nas interações dipolares deste sistema. Foi considerado a interação *Zeeman* ao incidir um campo magnético externo na superfície. Devido a geometria deste sistema, o campo de anisotropia H_A foi estudado para cada sistema de nanopilar. O modelo teórico para ajuste dos nossos parâmetros e análise do campo de anisotropia foram as equações de Kittel. Foram estudados para os pilares unitários as frequências de pico principal e secundário, a fim de obter informações sobre o campo de anisotropia da amostra. Para os picos primários, comparando com trabalhos da literatura notou-se que a resposta de ressonância ferromagnética vinha das laterais da estrutura no eixo z , nos picos secundários, os valores de H_A para campo perpendicular possuem grandes divergências de acordo com o modelo. Também foi possível observar que o ajuste para o campo de anisotropia melhora quanto maior for d . Devido as análises feitas para pilares unitários, não foram analisados os picos secundários para arranjos de pilares. Para os picos primários com campo perpendicular aplicado, foi observado que as equações de Kittel para ressonância ferromagnética não ajustam corretamente os valores de H_A . Na análise dos campos paralelos, procurou-se analisar a influência dos pilares vizinhos no valor de H_A . Utilizou-se um modelo considerando o fator de empacotamento do sistema. Neste modelo, foi comparado quando considera-se a cavidade no centro dos pilares e supondo-os pilares sólidos. A partir de comparação com resultados na literatura, o fator de empacotamento que melhor descreveu o sistema foi o primeiro, pois é adicionado mais efeitos dipolares ao sistema.

Palavras-chaves: ressonância ferromagnética; simulação ferromagnética; ferromagnetismo; campo de anisotropia.

LIST OF FIGURES

Figure 1 – The classification of structures containing nanoparticles by the shape. <i>0D</i> are structures which has high symmetry in their axis, <i>1D</i> have one axis longer than the other two generating elongated structures, <i>2D</i> have one axis smaller than the other two, which generates nanodisc or nanoroll. . . .	16
Figure 2 – (left) Sphere discretized by FDM, (right) Sphere discretized by Finite Element Method (FEM).	21
Figure 3 – Torque components exerted on the magnetization \vec{M} by rotational field \vec{H} (left). Motion of \vec{M} for constant \vec{H} using damping constant α (right). . . .	23
Figure 4 – Components of the external field H in the coordinates of the magnetization M	24
Figure 5 – Axes-to-sample setup for FMR frequency calculation.	27
Figure 6 – Demagnetization factors for FMR frequency (in System International of units and measurements (SI)) for simple forms and the arrow indicates the direction of applied field.	28
Figure 7 – Frequency versus external magnetic field corresponding to a magnetic system with uniaxial symmetry.	30
Figure 8 – (a) Magnetization varying in time for Ni solid squared pillar and his (b) Fast Fourier Transform (FFT) curve.	32
Figure 9 – Representation of discretization of a magnetic sample in a mesh of individual cells of volume $\Delta V = \Delta x \Delta y \Delta z$ (left). Each cell has uniform magnetization \vec{M} (right).	33
Figure 10 – Coordinate system for an array of nanowires.	34
Figure 11 – Definition of Nanopillars (NPs) a) solid and hollow with b) $d = 10$ nm and c) $d = 20$ nm.	36
Figure 12 – Geometry of 3x3 nanopillar array.	37
Figure 13 – OOMMF Graphical User Interface launcher.	38
Figure 14 – Fragment of nickel nanopillar simulation code in static regime.	41
Figure 15 – Fragment of nickel nanopillar simulation code in dynamic regime.	42
Figure 16 – Fragment of FMR script simulation	44

Figure 17 – Thin film geometry and application of \vec{H} field with 35.56° in the steady phase and 35° in dynamic stage with respect to the x-axis.	46
Figure 18 – a) $m_y(t)$ component of magnetization and b) power spectrum obtained using Fourier transform from the same region.	47
Figure 19 – Reproduction of thin film (BAKER et al., 2017) a) $M_y(t)$ component of magnetization and b) FFT from the same region.	48
Figure 20 – Isolated nanopillar with $d = 20$ nm a) $m_y(t)$ magnetization component and b) power spectrum obtained using Fourier transform from the same region indicated with primary and secondary peaks with 340 kA/m perpendicular applied field.	49
Figure 21 – Frequency versus external magnetic field of the main peak at ferromagnetic resonance for isolated: a) Solid nanopillar (NP) b) hollow NP with 10 nm cavity c) hollow NP with 20 nm cavity.	52
Figure 22 – Frequency versus external magnetic field of the secondary peak at ferromagnetic resonance for isolated: a) Solid nanopillar (NP) b) hollow NP with 10 nm cavity c) hollow NP with 20 nm cavity.	53
Figure 23 – Hysteresis cycle for: a) Solid nanopillar (NP). b) Hollow NP with 10 nm cavity. c) Hollow NP with 20 nm cavity.	56
Figure 24 – Nanopillar array with $d = 20$ nm and $a-D = 50$ nm a) $M_y(t)$ magnetization component and b) FFT showing maxima absorption frequencies from the same region indicated with primary and secondary peaks with 340 kA/m perpendicular field	58
Figure 25 – Frequency versus external magnetic field corresponding to a magnetic solid nanopillar array with uni-axial symmetry.	60
Figure 26 – Frequency versus external magnetic field corresponding to a magnetic nanopillar array hollowed with $D = 10$ nm in uniaxial symmetry.	62
Figure 27 – Frequency versus external magnetic field corresponding to a magnetic nanopillar array hollow with $D = 20$ nm in uniaxial symmetry.	63
Figure 28 – Ni squared nanopillar shape anisotropy field versus packing factor $P = \frac{D^2}{a^2}$.	65
Figure 29 – Ni squared nanopillar shape anisotropy field versus packing factor $P^* = \frac{D^2-d^2}{a^2}$	66
Figure 30 – Ni squared nanopillar array coefficient adjustments for packing factor P and P^*	67

LIST OF TABLES

Table 1 – Micromagnetic simulation softwares	20
Table 2 – Number of Cells for a Single Pillar	43
Table 3 – Number of Cells for a Pillar Array	43
Table 4 – Fitting of adjustment data from Pillar Array as function of d	64

LIST OF ABBREVIATIONS AND ACRONYMS

CGS	Centimetre–Gram–Second system of units
CPU	Central Processing Unit
EPR	Electron Paramagnetic Resonance
FDM	Finite Difference Method
FEM	Finite Element Method
FFT	Fast Fourier Transform
FMR	Ferromagnetic Resonance
GPU	Graphical Processing Unit
GUI	Graphical User Interface
LLG	Landau Lifshitz Gilbert
MFM	Magnetic Force Microscopy
MIF	Memory Initialization File
NIST	National Institute of Standards and Technology
NPs	Nanopillars
ODT	OpenDocument Text File format
OOMMF	The Object Oriented MicroMagnetic Framework
OS	Operational System
RAM	Random Access Memory
SI	System International of units and measurements
VNA	Vector Network Analyzer

LIST OF SYMBOLS

γ	Gyromagnetic Ratio
δ	Small Variation in the Variable
θ	Azimuthal Angle of Applied Field
ϕ	Polar Angle of Applied Field
α	Damping Factor
H_A	Anisotropy Field
\vec{H}	Applied Field
M_S	Saturation Magnetization
H_C	Coercivity Field
G	Gibbs Free Energy
g	Gibbs Free Energy per Volume
U_i	Potential Energy of a Magnetic Moment
\vec{m}_i	Magnetic Moment
\vec{H}	Magnetic Flux Density
\vec{M}	Magnetization Vector
μ_B	Bohr Magnetron
\vec{J}	Current Density
\hbar	Plank Constant
τ	Magnetic Torque
\vec{M}	Magnetization Vector
μ_0	Vacuum Permeability
S	Entropy

T	Temperature
dm	Magnetic Moment Differential
\overleftrightarrow{N}	Shape Tensor
ω	Resonance Frequency

CONTENTS

1	INTRODUCTION	15
2	FERROMAGNETIC RESONANCE AND SHAPE ANISOTROPY .	19
2.1	MICROMAGNETISM	21
2.2	FERROMAGNETIC RESSONANCE	24
2.2.1	Micromagnetic simulation in FMR	31
2.3	SHAPE ANISOTROPY IN MAGNETIC STRUCTURES	33
3	METHODOLOGY	36
3.1	OBJECT ORIENTED MICROMAGNETIC FRAMEWORK (OOMMF) . . .	38
3.1.1	Micromagnetic simulation code	40
3.2	FMR SIMULATION ITINERARY	42
3.2.1	Bash Script to execute static and dynamic codes in sequence . . .	43
3.2.2	Post-processing of simulated data	44
4	RESULTS	46
4.1	THIN FILM	46
4.2	ISOLATED NI NANOPILLAR RESULTS	48
4.2.1	Solid case for nanopillar	51
4.2.2	Solid pillar with hole of $d = 10$ nm	51
4.2.3	Solid pillar with hole of $d = 20$ nm	51
4.3	3X3 NI NANOPILLARS ARRAY	57
4.3.1	3x3 Ni solid pillar array	59
4.3.2	3x3 Ni hollowed with $d = 10$ nm pillar array	61
4.3.3	3x3 Ni hollowed with $d = 20$ nm pillar array	61
5	CONCLUSION	69
6	OUTLOOK	70
	REFERENCES	71
	ANNEX A – PAPERS RESULTING FROM THIS WORK	76

1 INTRODUCTION

The study of nanostructures has been growing, especially in recent years due to the needs of the technological sector in the construction of each time smaller equipment and the optimization of space inside electronic devices (APPELL, 2002; RUDI; LARSEN; JAKOBSEN, 1998). Nanotechnology deals with nano-scale ($\approx 10^{-9}$ m) objects and materials, that are useful in electronic devices that have applications in many areas, i. e., medicine, science materials, and physics. The nano characteristic permits the of study various properties because the short distances permits to reduce the energy lost in the electrons movement or studies in magnetical proprieties as domain walls and shape anisotropy field for example. In resume, nanomaterials have key physical characteristics imposed by the nano-objects part of it (BALL, 2001; REICH et al., 2003).

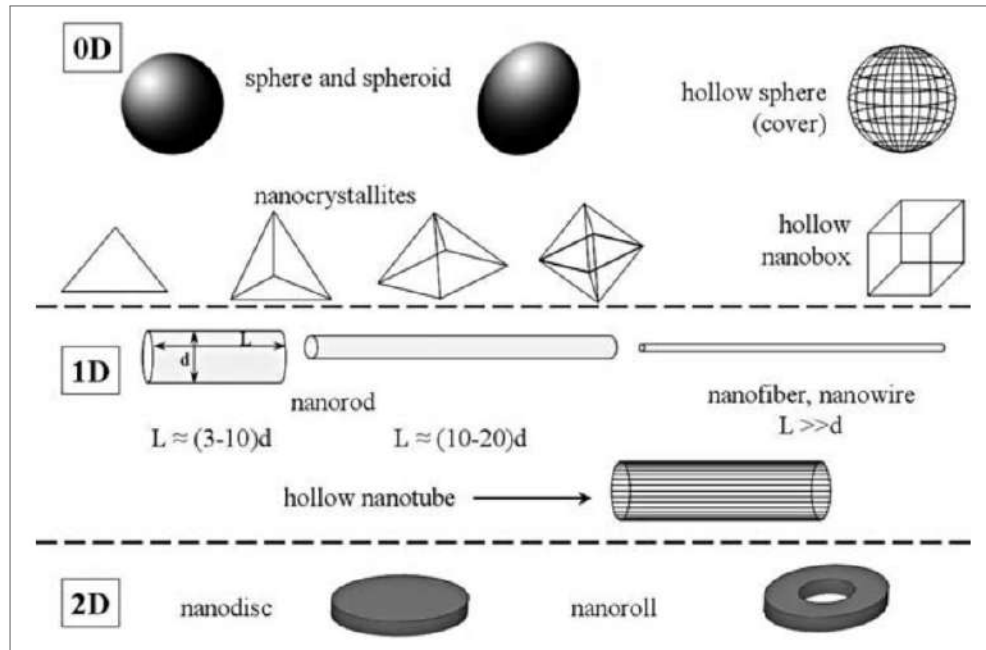
There are two kinds of nanomaterials, compact materials, and nanodispersions. The first type includes so-called nanostructured materials (MORIARTY, 2001), i.e., isotropic material in the macroscopic composition and consisting of attached nanometer-sized units as periodic repeating structural elements (GUSEV; REMPEL, 2004). Contrasting to nanostructured materials, nanodispersions include a homogeneous dispersion medium (vacuum, gas, liquid, or solid) and nanosized particles dispersed in this medium and isolated from each other. The distance between the nano-objects in these dispersions can vary over wide limits from below one hundred nanometers to rather more than fractions of a nanometer (GUBIN, 2009).

The study of nanoparticles has a great scientific interest because they present characteristics that connect bulk materials and molecules and structures at an atomic level. The term "cluster", is used to designate small nanoparticles with sizes comparable to 1 nm.

Figure 1 shows that nanorods and nanowires present a quasi-one-dimensional behavior due to the higher symmetry in one direction (1D) of these nano-objects. These systems present a principal axis where one dimension is larger in magnitude than the other two dimensions, all dimensions are in nanoscale. Analyzing the group of two-dimensional confinement objects (2D) which includes planar structures – nanodisks, thin-film magnetic structures, and magnetic nanoparticle layers, see Figure 1, it is possible to see that two dimensions are clearly greater than a third dimension, which is in the nanometer range also. The unique magnetic properties are usually inherent in the particles with a core size of 2–30 nm. The magnetic properties of these structures are unique and usually intrinsic in particles with a core size of 2–30 nm. In

the case of magnetic nanoparticles, this value coincides with the size (or less) of a magnetic domain in many magnetic bulk materials.

Figure 1 – The classification of structures containing nanoparticles by the shape. *0D* are structures which has high symmetry in their axis, *1D* have one axis longer than the other two generating elongated structures, *2D* have one axis smaller than the other two, which generates nanodisc or nanoroll.



Source: GUBIN (2009)

Some applications of nanostructures can be found in medicine (REICH et al., 2003) by using nanomaterials to perform cell biopsy, besides that, some improvements in the scanning probe microscopes precision were also made (DAI et al., 1996). The implementations of nanomaterials also formed the basis for nanoscale tweezers that can rearrange microscopic particles in the structures (KIM; LIEBER, 1999), furthermore many applications on logic gates (RUECKES et al., 2000; DERYCKE et al., 2001).

Magnetic nanostructures have been extensively studied by many authors and it is known that magnetic materials have a high shape correlation with coercivity and remanence. Guerra *et al.* in his work with nanoshell array showed the dependence of coercivity and remanence with the arrangement of structure (isolated nanoshell, chained nanoshell, and hexagonal array of nanoshell) with the magnetization reversal process that affects the coercivity due to shape anisotropy (DÁVILA, 2019) and showed that inter-pillar dipolar interaction is the reason for modification in the coercivity (GUERRA et al., 2021). Those results are also theoretical predicted in literature by some authors (GUIMARÃES; OLIVEIRA, 1998; REZENDE, 2020; YALÇIN, 2013; BERTOTTI, 1998).

Due to the difficulty in getting these materials and the expensive measuring and preparation equipments, micromagnetic simulation becomes a cheap and efficient way to conduct the research. The micromagnetic simulation method consists in discretizing the Landau Lifshitz Gilbert (LLG) equation. This equation is applied to each magnetizing element in a unit cell. Discretization can be done in two ways, using the FDM and FEM method which works better for Cubic and Spheroidal surfaces respectively.

One way to analyze the results, in addition to using the hysteresis curves to characterize the samples, is to analyze the FMR frequency spectrum in each structure. From the analysis of the field and frequency parameters, it is possible to obtain the arrangement interference in each of the particles by analyzing the packing factor or comparing the data generated for the unit pillar with the theoretical result.

ENCINAS-OROPESA *et al.* studied nickel nanowires dipolar interaction by using FMR and they found that the dipolar coupling can be characterized by FMR technique and the limit of isolated nanowire and interacting wire can be found by changing the porosity (ENCINAS-OROPESA *et al.*, 2001). In other work, DEMAND *et al.* analyzed Kittel equation with experimental data to obtain the anisotropy field and used the equations from the work of Hernandez *et al.* to obtain each magnetic nanowire fabricated packing factor (HERNÁNDEZ; REZENDE; AZEVEDO, 2008; DEMAND *et al.*, 2002). BAKER *et al.* suggest a method to simulate FMR for a thin film of permalloy (BAKER *et al.*, 2017). The method can be replied as done by SILVA *et al.* did to study the anisotropy in hollow nanopillars (SILVA; GUERRA; PADRÓN-HERNÁNDEZ, 2021). The results imply the dipole effects due to the inner and outer faces are reverted in the increase of the uniaxial anisotropy.

Geometry analysis response in some works shows (SILVA; GUERRA; PADRÓN-HERNÁNDEZ, 2021; DEMAND *et al.*, 2002) that sample's shape is important because it generates an anisotropy field (H_A) opposite to the applied field (\vec{H}). In addition to the shape, the influence of nearing structures affects the geometry so analyzing isolated objects or disposed in an array influences the system dipole response. In structures with one axis great than the others, the effect of a cavity in the center of each structure must be analyzed because it introduces more dipole interactions. ESCRIG *et al.* noted that the increase of radius in a nanowire array decreases its coercivity (ESCRIG *et al.*, 2008). SILVA *et al.* also reported that for greater hollows in nanopillar the anisotropy field increases, causing the coercivity field to increase (SILVA; GUERRA; PADRÓN-HERNÁNDEZ, 2021).

This dissertation work is described in 5 chapters, Chapter 1 addresses the need to under-

stand the basic concepts of magnetism, where the ferromagnetic response comes from, and how we can analyze these results from the analysis of the FMR spectrum. In addition, it also covers the concepts of micromagnetic simulation and covers examples of these simulations to obtain the FMR spectrum. Chapter 2 analyzes the equations that serve as a model for our phenomenological description from basic principles of magnetism as the coherent rotation model. Furthermore, it provides means to discuss the interaction between the studied column arrangement based on its packing factor. Chapter 3 details the methodology to make the structure simulations and how the structures were assembled in the files that are provided to the simulation package. In addition, the parameters provided for the code are described, as well as a bash script that was needed to simulate the resonance in the static phase simulation could be inserted in the dynamic phase, giving rise to resonance. In Chapter 4, the results obtained by simulation initially for a thin film are analyzed, according to the work in the literature (BAKER et al., 2017). After analyzing the obtained data and comparing it with the results of the original paper, the results for singular squared pillars according to the adjustment made by the Kittel equations are also verified. Finally, we studied the squared NPs array in a 3x3 arrangement to verify the influence of neighbors on the magnetic properties of this system from the analysis of the packing factor. Chapter 5 concludes all the analysis and shows some perspectives to better understand the results shown.

2 FERROMAGNETIC RESONANCE AND SHAPE ANISOTROPY

Micromagnetic studies are motivated by the need of reducing scales whether for use in the human body or to remain more physical space for other components in a computer and other applications. Nowadays technological companies are in search of reducing scales in their processors. The new generation of chipsets from QualcommTM have transistors of 5 nm inter-distance. These chipsets consume less energy, permitting to have more transistors in the system electronics and faster processing because reducing distances, reduces the electron traveling distance, which reduces the energy losses (MOORE, 2020; QUALCOMM, 2021). Magnetic materials have large applicability. They are useful in technological and biomedical applications (REICH et al., 2003). In other work, RUDI *et al.* described that paramagnetic beads could be used for cell concentration and DNA purification (RUDI; LARSEN; JAKOBSEN, 1998). Also, another utilization of micromagnetics is the magnetic recording based on properties such as remanence magnetization (CULLITY; GRAHAM, 2011).

Magnetic materials have a high correlation between shape and magnetical properties as coercivity and remanence (DÁVILA, 2019; GUERRA et al., 2021), therefore, geometry studies using different types of ferromagnetic structures are useful and has been of great interest for material science, physics, chemistry, geology, biology, and medicine (TEHRANI; KIM; YOON, 2014). Ferromagnetic systems present spontaneous magnetization due to parallel alignment of spins. The ferromagnetic coupling originates from the spins of d-electrons. In recording media, the objective is to fabricate high-permeability and low-coercivity magnetic materials capable of operating at reasonably high frequencies, so the searching for materials with these properties is essential. To obtain those properties, for example, parameters of the studied material must be adjusted.

Nowadays, the difficulty of carrying out some experimental processes, *e.g.*, lithography, and the difficulty to find out analytical solutions for many micromagnetic systems because of its exhausting calculus that can be complicated depending on the geometry. Another difficulting factor is the resolution of LLG equation which is a partial differential equation and presents an analytical solution just in a few cases, *e.g.* single domain rotation for one ellipsoid (STONER; WOHLFARTH, 1948). The situations mentioned above make the use of micromagnetic simulation essential. Micromagnetic simulations are much cheaper and can be reproduced in computers based on their Random Access Memory (RAM) or Graphical Processing Unit (GPU).

Simulations can take place using the finite element method FEM or the finite difference method FDM. These methods have different applicability and depend on the physical parameters of interest. There are many options for simulation packages, as shown in Table 1. Free open-source packages are the most used to save costs. The main differences in the simulation packages are in the fact that the research works with dedicated memory to the process with the aid of GPU or with RAM, using RAM simulators packages makes the calculations up to 8 times slower compared to GPU simulators (KAKAY; WESTPHAL; HERTEL, 2010).

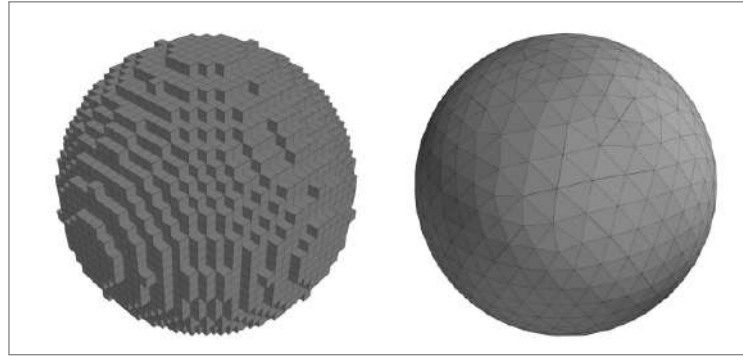
Table 1 – Micromagnetic simulation softwares

Software	Open source	Method	Source website
OOMMF	Free	FDM	math.nist.gov/oommf/
Nmag	Free	FEM	nmag.soton.ac.uk/nmag/
Magpar	Free	FEM	magnet.atp.tuwien.ac.at/sc_holz/magpar
Mumax	Free	FEM	mumax.github.io/
Fidimag	Free	FDM	computationalmodelling.github.io/fidimag/
LLG Simulator	Paid	FDM	llgmicro.home.mindspring/
MicroMagus	Paid	FDM	micromagus.de/

Source: Elaborated by the author (2021)

For FEM, the Nmag is mostly used (FISCHBACHER et al., 2007) since this software doesn't use GPU and is free of charge. For FDM, I highlight the OOMMF (DONAHUE; DONAHUE, 1999), which has applications in FMR simulations and also in the characterization of magnetical reversion in structures. The main difference between the two methods is their applicability in geometries. FDM is more accurate for cubic structures while FEM works best for tetrahedral structures. The magnetization in OOMMF is associated with the center of the cubic cells while in Nmag is associated with the corners of the tetrahedral (MAHALINGAM; MANIKANDAN; AROCKIARAJ, 2019). The main advantage of FDM is that the demagnetizing field can be calculated directly via Fourier transform techniques but when the geometry presents a spherical geometry, the system is represented spatially as a staircase pattern as it can be seen in Figure 2, *i.e.*, reduced precision for spherical structures. In FEM, spherical and curved geometries are spatially resolved more accurately, on the other hand, flat geometries (thin film) require more memory to perform.

Figure 2 – (left) Sphere discretized by FDM, (right) Sphere discretized by FEM.



Source: BOARDMAN (2005)

2.1 MICROMAGNETISM

To understand the dynamics of magnetization it is necessary to consider the interaction energy between a magnetic moment \vec{m} and magnetic field \vec{B} , as described in the literature (GUIMARÃES; OLIVEIRA, 1998; REZENDE, 2020; KRONMÜLLER; PARKIN, 2007):

$$U_i = -\vec{m}_i \cdot \vec{B}, \quad (2.1)$$

where the magnetic moment can be defined by:

$$\vec{m}_i = -g\mu_B\vec{J}. \quad (2.2)$$

Equation 2.1 means that the minimum energy is obtained for \vec{m}_i and \vec{B} aligned, while the maximum will happen if the same vectors are anti-parallel. Equation 2.2 is the definition of the magnetic moment that takes into account the total angular momentum $\hbar\vec{J}$, which is the sum of orbital $\hbar\vec{L}$ and spin $\hbar\vec{S}$ angular momenta (SAKURAI; COMMINS, 1995). The Bohr magneton μ_B and spectroscopic splitting factor g are also included in its definition. If an external field is applied to a magnetic sample, the moments experience a torque:

$$\vec{\tau} = \vec{m}_i \times \vec{B}, \quad (2.3)$$

there is a correlation between magnetization and applied field, where the greater the angle between the vectors, the larger the torque experienced by the magnetization. From Newton's 2nd law of motion, it's known that torque is generated by the derivative of angular momentum in time:

$$\frac{d(\hbar\vec{J})}{dt} = \vec{\tau} = \vec{m}_i \times \vec{B}, \quad (2.4)$$

substituting 2.2 in 2.4 is found:

$$\frac{d\vec{m}_i}{dt} = -\gamma\vec{m}_i \times \vec{B}, \quad (2.5)$$

where $\gamma = \frac{g\mu_B}{\hbar}$ is the gyromagnetic ratio. As it is easier to work with macroscopic quantities, it is defined the magnetization vector, which is the magnetic moment per unit of volume:

$$\vec{M} = \frac{1}{V} \sum_i \vec{m}_i. \quad (2.6)$$

After analyzing the contribution of each cell, the Equation 2.4 can be written as:

$$\frac{d\vec{M}}{dt} = -\gamma\vec{M} \times \vec{B}, \quad (2.7)$$

using the relation $\vec{B} = \mu_0(\vec{H} + \vec{M})$ in the SI, where \vec{H} is the magnetic field strength and μ_0 the magnetic permeability of the vacuum, it becomes to:

$$\frac{d\vec{M}}{dt} = -\gamma\mu_0\vec{M} \times (\vec{H} + \vec{M}),$$

since, the second term of the right side cancels itself because they are parallel ($\vec{M} \times \vec{M} = 0$), we have:

$$\frac{d\vec{M}}{dt} = -\gamma\mu_0\vec{M} \times \vec{H}. \quad (2.8)$$

This result is known as the Landau-Lifshitz equation and describes the change in magnetization over time in the absence of damping (LANDAU; LIFSHITZ, 1992).

To create a more accurate system, it is necessary to make the system's energy decrease over time. Reproducing the work of Gilbert and replacing the previous field for \vec{H} and a *damping field depending on magnetization*, so that over time the system reaches equilibrium (GILBERT, 2004):

$$\vec{H} \rightarrow \vec{H} - \frac{\alpha}{\gamma\mu_0|\vec{M}|} \frac{d\vec{M}}{dt}, \quad (2.9)$$

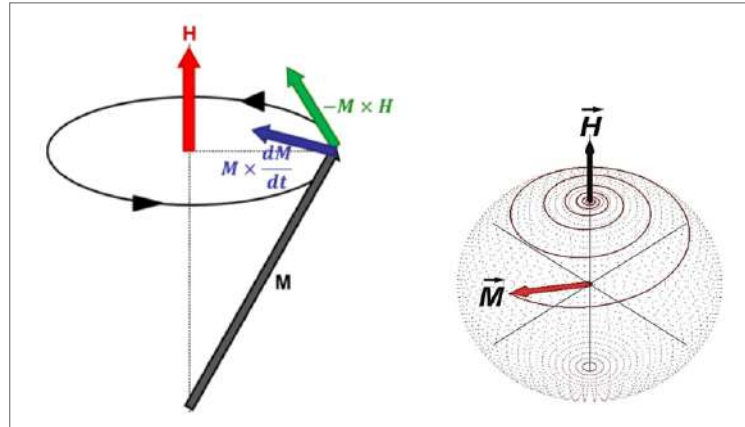
where α is the Gilbert damping constant and $|\vec{M}| = M_S$ is the saturation magnetization. Substituting 2.9 into 2.8 we find:

$$\frac{d\vec{M}}{dt} = -\gamma\mu_0\vec{M} \times \vec{H} + \frac{\alpha}{M_S} \vec{M} \times \frac{d\vec{M}}{dt}. \quad (2.10)$$

To remove the dependence on the magnetization variation $\frac{d\vec{M}}{dt}$ in Equation 2.10, it is used the Equation 2.8, to get:

$$\frac{d\vec{M}}{dt} = -\gamma\mu_0\vec{M} \times \vec{H} + \frac{\alpha}{M_S} \vec{M} \times \vec{M} \times \vec{H}. \quad (2.11)$$

Figure 3 – Torque components exerted on the magnetization \vec{M} by rotational field \vec{H} (left). Motion of \vec{M} for constant \vec{H} using damping constant α (right).



Source: YALÇIN (2013)

Both Expressions 2.10 and 2.11 are the Landau-Lifshitz-Gilbert equation, but in Equation 2.10, the precession terms are uncoupled. This equation shows that the system loses energy until it reaches the equilibrium state, where \vec{M} is parallel to \vec{H} , as shown in Figure 3.

Micromagnetics is based on the idea of an effective field \vec{H} acting on the macroscopic local magnetization, defined as the negative variational derivative of the total Gibbs' free energy, G , from the first law of thermodynamics (KARDAR, 2007), where S is the entropy, and T the temperature of the system:

$$dG = -SdT - \vec{B} \cdot d\vec{M}. \quad (2.12)$$

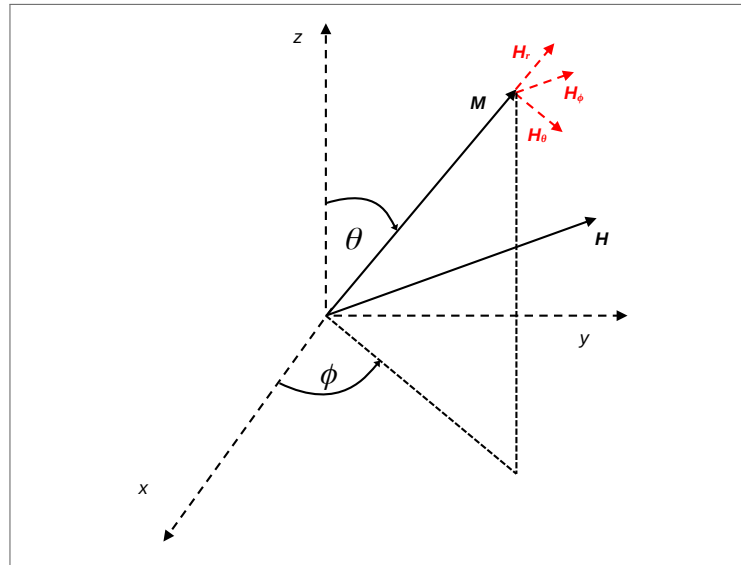
Considering the magnetic field from inside of structure, $\vec{B} = \mu_0(\vec{H} + \vec{M})$, the Equation 2.12 can be written, considering $\vec{m} = \frac{\vec{M}}{M_S}$ to be the normalized magnetization and fixing the temperature then consider the effective field to be:

$$\vec{H} = -\frac{1}{\mu_0 M_S} \frac{\delta G}{\delta \vec{m}}.$$

For the simulations we considered the exchange energy term, since it is a property each ferromagnetic material, the demagnetizing term to account for the geometry structure, and the Zeeman energy for the effect of applied field:

$$G = E_{exchange} + E_{demag} + E_{Zeeman}. \quad (2.13)$$

Figure 4 – Components of the external field H in the coordinates of the magnetization M .



Source: Elaborated by the author (2021)

2.2 FERROMAGNETIC RESSONANCE

Almost every parameter of a ferromagnet can be obtained using ferromagnetic resonance (YALÇIN, 2013). The spectroscopic splitting factor, anisotropy field, symmetry axis, and resonance frequency could be obtainable from FMR spectra. By using the Equations 2.5 and 2.6, we can obtain the Equation 2.8, which describes the magnetization behavior in a non-damping medium. Using the spherical coordinate system (ARFKEN; WEBER, 1999) for the magnetization and external field (Figure 4) and writing the \vec{H} field components in the \vec{M} system, it is found:

$$\vec{H}_r = H_x \sin \theta \cos \phi \hat{x} + H_y \sin \theta \sin \phi \hat{y} + H_z \cos \theta \hat{z}, \quad (2.14)$$

$$\vec{H}_\theta = H_x \cos \theta \cos \phi \hat{x} + H_y \cos \theta \sin \phi \hat{y} - H_z \sin \theta \hat{z}, \quad (2.15)$$

$$\vec{H}_\phi = -H_x \sin \phi \hat{x} + H_y \cos \phi \hat{y}. \quad (2.16)$$

Using the Equation 2.8 it is found:

$$\begin{pmatrix} \dot{M}_x \\ \dot{M}_y \\ \dot{M}_z \end{pmatrix} = -\gamma \begin{pmatrix} \hat{i} & \hat{j} & \hat{k} \\ M_x & M_y & M_z \\ H_x & H_y & H_z \end{pmatrix}. \quad (2.17)$$

Using $\dot{M}_i = \frac{dM_i}{dt}$, Equation 2.17 can be rewritten as:

$$\begin{aligned}\dot{M}_x &= -\gamma(M_y H_z - M_z H_y), \\ \dot{M}_y &= -\gamma(M_z H_x - M_x H_z), \\ \dot{M}_z &= -\gamma(M_x H_y - M_y H_x).\end{aligned}\tag{2.18}$$

Writing \vec{M} in spherical coordinates and remembering that $|M|$ is constant, we obtain:

$$\dot{r} = 0, \tag{2.19}$$

$$\dot{\theta} = \gamma(H_y \cos \phi - H_x \sin \phi) = \gamma H_\phi, \tag{2.20}$$

$$\dot{\phi} = \frac{\gamma}{\sin \theta \cos \phi} (H_z \sin \theta \cos \phi - H_x \cos \theta - H_\phi \sin \phi \cos \theta) = -\frac{\gamma}{\sin \theta} H_\theta. \tag{2.21}$$

Now looking at the Gibbs free energy function divided by volume $g(M, T)$, it can be written:

$$dg = \frac{\partial g}{\partial M} dM + \frac{\partial g}{\partial T} dT,$$

where $(\frac{\partial g}{\partial M})_T = -H_M$ which is the field along the magnetization direction. The magnetization has a dependence on $M(\theta, \phi)$ due to the coherent rotation model adopted. So the Gibbs Energy can be written as $g(M(\theta, \phi), T)$. By using the chain rule for partial derivative, we find:

$$\begin{aligned}\frac{\partial g}{\partial \theta} &= \frac{\partial^2 g}{\partial \theta^2} \delta \theta + \frac{\partial^2 g}{\partial \theta \partial \phi} \delta \phi, \\ \frac{\partial g}{\partial \phi} &= \frac{\partial^2 g}{\partial \phi^2} \delta \phi + \frac{\partial^2 g}{\partial \theta \partial \phi} \delta \theta.\end{aligned}\tag{2.22}$$

In those equations it was used $\frac{\partial g}{\partial \phi} = g_\phi$ and $\frac{\partial g}{\partial \theta} = g_\theta$. Using the relations of spherical coordinates, it can be written $\frac{g_\theta}{M} = -H_\theta$ and $\frac{g_\phi}{M \sin \phi} = -H_\phi$. In case of FMR, the magnetic moments vary little as a function of the angles θ and ϕ when the field's application angle is changed (Subsection 2.2.1). Assuming that, it can be written $\theta \rightarrow \delta \theta$ and $\phi \rightarrow \delta \phi$ in Equations 2.20 and 2.21 and then it can be conclude that:

$$\begin{aligned}\frac{d(\delta \theta)}{dt} &= \gamma H_\phi, \\ \frac{d(\delta \phi)}{dt} &= -\gamma \frac{H_\theta}{\sin \theta}.\end{aligned}\tag{2.23}$$

In Equation 2.23 it is possible to put in the right side, the Equation 2.22 to find a system of coupled equations. To solve this problem, harmonic solutions are proposed in literature where θ and ϕ have same frequency due to the coherent rotation.

$$\begin{aligned}\delta \theta &= A e^{i\omega t}, \\ \delta \phi &= B e^{i\omega t}.\end{aligned}\tag{2.24}$$

Substituting Equation 2.24 in 2.23, we find:

$$\begin{cases} B(\frac{Mi\omega \sin \theta}{\gamma}) - g_{\theta\phi} = Ag_{\theta\theta}, \\ A(\frac{Mi\omega \sin \theta}{\gamma}) + g_{\theta\phi} = -Bg_{\phi\phi}. \end{cases}$$

Solving the system of equations above, it can be found:

$$\omega = \frac{\gamma}{M \sin \theta} \sqrt{g_{\theta\theta}g_{\phi\phi} - g_{\theta\phi}^2}. \quad (2.25)$$

Considering a uniaxial sample, the exchange term of Equation 2.13 is null because in the resonance all momenta are coupled. For the other contributions of the energy, it can be shown that:

$$G_{demag} = -\frac{V}{2} \vec{M}_S \overleftrightarrow{N} \vec{M}_S, \quad (2.26)$$

$$G_{Zeeman} = -\vec{M} \cdot \vec{H}V. \quad (2.27)$$

Equations 2.26 and 2.27 can be written divided by V to be used in Equation 2.25. The Equation 2.26 represents how the geometry affects the energetic equilibrium. The shape tensor \overleftrightarrow{N} can be diagonalized by using of the demagnetizing factors¹ and their values for high symmetry geometries can be found in Figure 6 in SI and the magnetization must be written in spherical coordinates. Executing this last procedure, it can be found:

$$g_{demag} = -\frac{M_S^2}{2} \begin{pmatrix} \sin \theta \cos \phi & \sin \theta \sin \phi & \cos \theta \end{pmatrix} \begin{pmatrix} N_x & 0 & 0 \\ 0 & N_y & 0 \\ 0 & 0 & N_z \end{pmatrix} \begin{pmatrix} \sin \theta \cos \phi \\ \sin \theta \sin \phi \\ \cos \theta \end{pmatrix}. \quad (2.28)$$

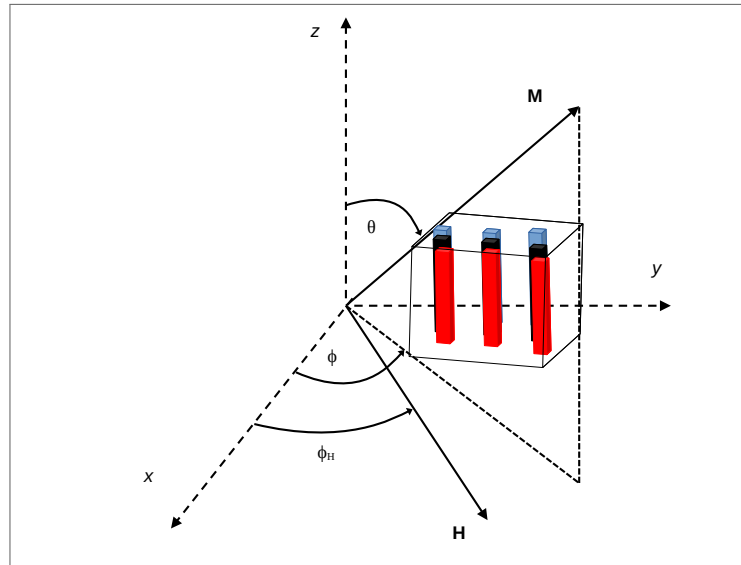
In this work, it is studied isolated NPs in Figure 11 and NPs Array in Figure 12 layed in x direction, so putting in the shape tensor $N_x = 0$, $N_y = \frac{1}{2}$ and $N_z = \frac{1}{2}$ approximating for a cylinder as the parameters of Figure 6. Solving the Equation 2.28 it can be found:

$$g_{demag} = -\frac{M_S^2}{2} \left(\frac{\sin^2 \theta \sin^2 \phi}{2} + \frac{\cos^2 \theta}{2} \right). \quad (2.29)$$

Rewriting the above result as a function of the uniaxial anisotropy constant, where $K_1 = \frac{H_A M_s}{2}$, where H_A is the shape anisotropy field, which represents the hypothetical field that would be able to set the magnetization perpendicular to the easy axis (KOOLS; MOREL, 2004; YALÇIN, 2013). Equation 2.29 can be written as:

$$g_{demag} = \frac{H_A M_S}{2} (\sin^2 \theta \sin^2 \phi + \cos^2 \theta). \quad (2.30)$$

Figure 5 – Axes-to-sample setup for FMR frequency calculation.



Source: Elaborated by the author (2021)

Considering Figure 5, which represents how the H field was applied to the sample. Looking at the figure above, the Equation 2.27 can be determined in spherical coordinates:

$$g_{Zeeman} = -MH(\sin\theta \cos\phi + \sin\theta \sin\phi + \cos\theta)(\cos\phi_H \sin\theta_H + \sin\phi_H \sin\theta_H + \cos\theta_H). \quad (2.31)$$

From Figure 5 it can be found that $\theta_H = \frac{\pi}{2}$ is the equilibrium angle and after some algebra, the result can be found:

$$g_{Zeeman} = -MH \cos(\phi - \phi_H). \quad (2.32)$$

Since the Equations 2.30 and 2.31 are the only remaining energy terms, the Gibbs function divided by volume can be written as:

$$g = \frac{MH_A}{2} \sin^2\phi - MH \cos(\phi - \phi_H). \quad (2.33)$$

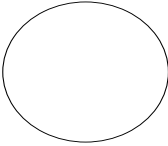
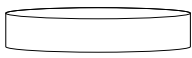



Now, using g_ϕ and g_θ from the Equation 2.33, from the magnetic field conditions H in equilibrium, it can be found that $g_\theta = 0$ and $g_\phi = 0$ therefore:

$$H_A \sin(2\phi) + 2H \sin(\phi - \phi_H) = 0. \quad (2.34)$$

The Equation 2.34 can be used to define the equilibrium condition for ϕ_H . Derivating this equation again to achieve the components $g_{\theta\theta}$, $g_{\phi\phi}$ and $g_{\theta\phi}$ using the condition of $\theta_H = \frac{\pi}{2}$ it

¹ $N_x + N_y + N_z = 1$ (SI)

Figure 6 – Demagnetization factors for FMR frequency (in SI) for simple forms and the arrow indicates the direction of applied field.

Sample shape and field direction	Demagnetizing factors	ω_0/γ
	$N_x = N_y = N_z = 1/3$	H
	$N_x = N_y = 0$ $N_z = 1$	$H - M$
	$N_z = N_x = 0$ $N_y = 1$	$[H(H + M)]^{1/2}$
	$N_z = 0$ $N_y = N_x = 1/2$	$H + M/2$
	$N_y = 0$ $N_x = N_z = 1/2$	$[H(H - M/2)]^{1/2}$

Source: REZENDE (2020)

can be obtained:

$$g_{\theta\theta} = MH_A \cos^2 \phi + MH \cos(\phi - \phi_H), \quad (2.35)$$

$$g_{\theta\phi} = 0, \quad (2.36)$$

$$g_{\phi\phi} = MH_A \cos(2\phi) + MH \cos(\phi - \phi_H). \quad (2.37)$$

Now finally setting the Equations 2.35 and 2.37 into Equation 2.26, and using the equilibrium condition, we have:

$$\frac{\omega^2}{\gamma^2} = (H_A \cos(2\phi) + H \cos(\phi - \phi_H))(H_A \cos^2 \phi + H \cos(\phi - \phi_H)). \quad (2.38)$$

The above result was first deduced by Charles Kittel (KITTEL, 1947) and shows that FMR frequencies depends on the sample format, the material used and the applied field. Figure 6

indicates how the format influences the frequency in simple forms. In the case of a field parallel to the sample, setting $\phi = 0$ and $\phi_H = 0$ it can be found:

$$\frac{\omega}{\gamma_{\parallel}} = H_A + H. \quad (2.39)$$

For the perpendicular case, Equation 2.34 can be used to find that the equilibrium condition is $\sin \phi = \frac{H}{H_A}$, where is known that $H < H_A$ because $-1 < \sin \phi < 1$. Applying this condition in Equation 2.38:

$$\frac{\omega^2}{\gamma^2} = H_A \left(1 - 2\frac{H}{H_A} + \frac{H^2}{H_A^2}\right) \left(H_A \left(1 - \frac{H^2}{H_A^2}\right) + \frac{H^2}{H_A}\right)$$

Equation 2.39 can be easily solved to find:

$$\frac{\omega}{\gamma_{\perp}} = \sqrt{H_A^2 - H^2} \quad \text{if } H < H_A. \quad (2.40)$$

The other condition ($H > H_A$) cannot be used due to function $\sin \phi$ restriction. For the last case using $\phi = \phi_H = \frac{\pi}{2}$ to get:

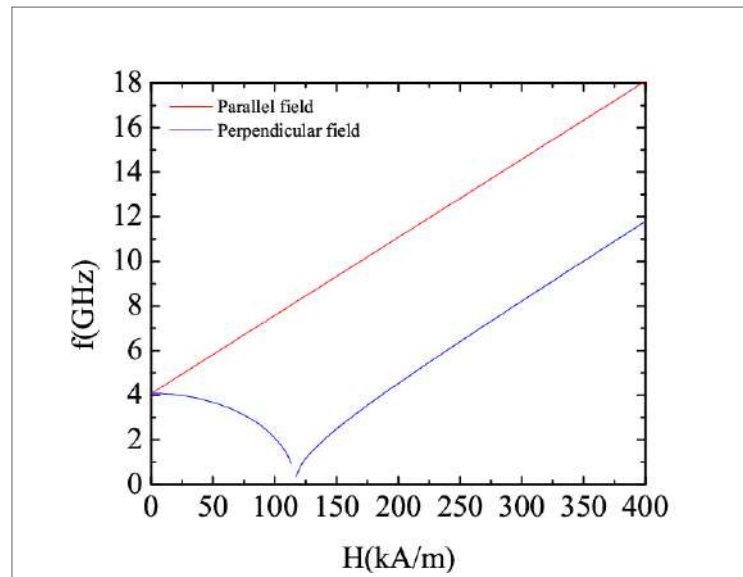
$$\frac{\omega}{\gamma_{\perp}} = \sqrt{H(H - H_A)} \quad \text{if } H > H_A. \quad (2.41)$$

Kittel's equations have many applications in the literature. For example, in the work of Dao *et al.* which calculated the dynamic susceptibility of patterned cobalt and Permalloy pillars with a diameter of 50 nm and different pillar heights using micromagnetic simulations. The resonance modes obtained from these simulations were compared to the results obtained from an analytical solution (Equation 2.38) for spheroids (DAO *et al.*, 2004). After that, Neudecker *et al.* propose a experimental study comparing frequency, field and time domain ferromagnetic resonance in four methods. This work used the equations described above to adjust the experimental data and compare the results (NEUDECKER *et al.*, 2006). Curiale *et al.* investigate the dynamic response for magnetic nanoparticles by using Kittel's equation and calculating the magnetic susceptibility (CURIALE *et al.*, 2008). Raposo *et al.* experimentally investigate the FMR in low interacting permalloy nanowire array and used the ferromagnetic resonance equations to adjust his obtained data (RAPOSO *et al.*, 2016). Yang *et al.* studied the static and dynamic magnetization of gradient FeNi alloy nanowire by considering Kittel's equation. In their study was considered a hexagonal array of nanowires and the analyzed parameters considered was the gradient FeNi and homogeneous FeNi alloy (YANG *et al.*, 2016).

Similar treatments of simulated FMR were obtained by Wagner *et al.*. Using MuMax³ they found the absorption spectra of permalloy and the excitation response from the sample. The

work was performed by a mimic of the experimental conditions and after that, they proceed to qualitatively study weakly nonlinear ferromagnetic resonance (WAGNER et al., 2021). Saavedra *et al.* studied the dynamic susceptibility (similar to Dao *et al.*) of modulated permalloy nanowires of 1- μm long and 50 nm diameter using micromagnetic simulations. They investigate how the modulus changes the nanowire susceptibility by analyzing the resonance modes and the resonance frequencies (SAAVEDRA et al., 2019). Lenz *et al.* investigates the magnetization dynamics of individual Fe-filled multiwall carbon-nanotubes, grown by chemical vapor deposition and compared to their micromagnetic simulations. In their simulated analysis by using Kittel's equation, they found similar results to Figure 7 where the left side of the blue line to the perpendicular field was attributed to unaligned modes, i.e., the external field is not yet strong enough to pull the magnetization in its direction (LENZ et al., 2019).

Figure 7 – Frequency versus external magnetic field corresponding to a magnetic system with uniaxial symmetry.



Source: Elaborated by the author (2021)

Equation 2.39, means the parallel applied field (red line) and Equations 2.40 and 2.41 the perpendicular applied field (blue line) in relation to the principal axis, which generates Figure 7. Piroux analyses different results in literature for experimental and simulated nanowire array varying their porosity and showed the results of parallel and perpendicular field switching their positions. His analysis was performed by using the equations for parallel (Equation 2.39) and perpendicular (Equations 2.40 and 2.41) field (PIRAUX, 2020).

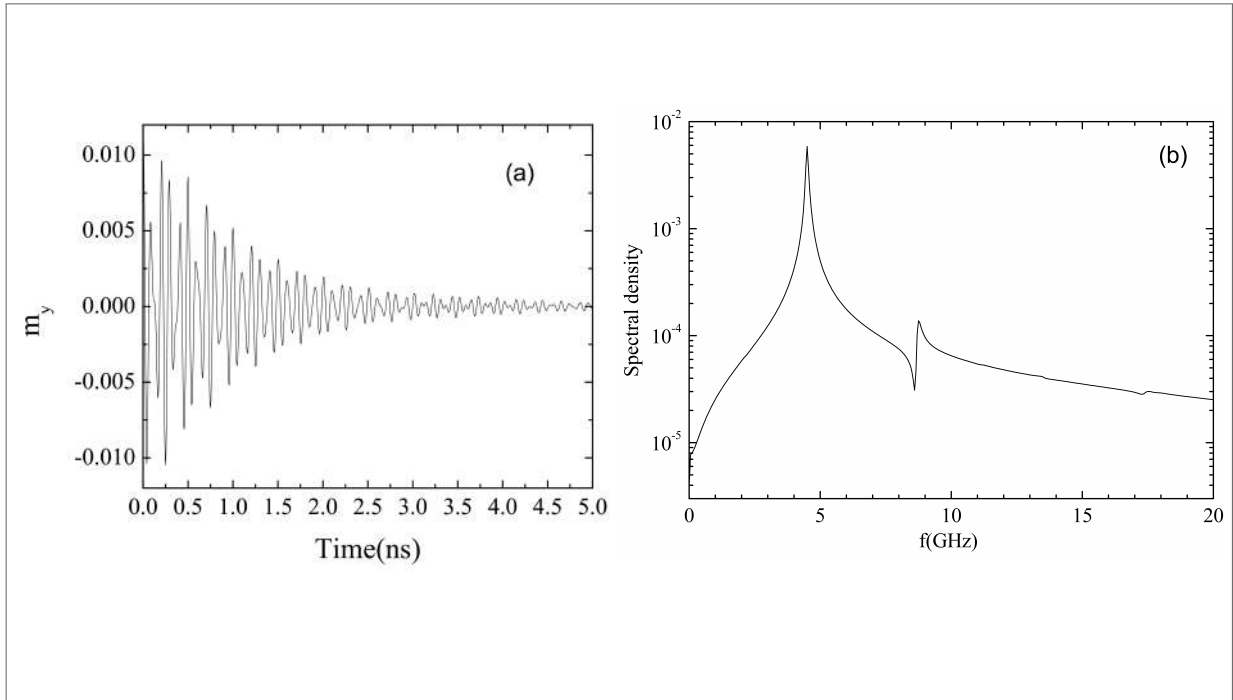
2.2.1 Micromagnetic simulation in FMR

Previously, it was shown that the LLG equation is not easily solved for a huge number of systems. As a direct consequence, the complexity of common problems requires the use of micromagnetic simulation packages. According to BAKER *et al.*, there are three methods to do the FMR micromagnetic simulation (BAKER *et al.*, 2017):

1. For every frequency ω , the micromagnetic simulator computes the time evolution of the system's magnetization after the transient dynamics have been damped and steady magnetization precession obtained. An application of a time-dependent periodic sinusoidal magnetic microwave field of fixed frequency ω is needed to determine the magnetization precession amplitude in response to the system. Just a micromagnetic simulation software that supports a time-dependent external magnetic field can be used in this case.
2. Ringdown method (MCMICHAEL; STILES, 2005): this method consists of perturbing the magnetic system from its equilibrium state using a short-duration and sufficiently soft excitation, simulation, after those procedures, the magnetization dynamics is recorded. The results from this first step are the varying time magnetization and performing the Fourier transform in time it is possible to obtain the resonance frequencies, respectively on the recorded data. This method permits to determine efficiently the eigenmodes of the system and can be done using a script coupled with the OOMMF package.
3. Eigenvalue method (D'AQUINO *et al.*, 2009): rather than simulating the time evolution of the system's magnetization as in methods 1 or 2, the problem is represented as an eigenvalue problem, whose solutions provide the eigenvalues and the eigenvectors of the system which are the frequencies and the mode shape respectively. This method requires specific software that is not widely available.

The OOMMF package permits to the use of the second alternative. After running the program, the magnetization data varying in time are taken, Figure 8a), and an FFT must be performed, as Figure 8b) to obtain the maximum resonance frequency for each external field applied. Subsequently, analyzing the frequency dependence with the field, to find H_A and the other parameters of Equation 2.39 for a parallel field and Equations 2.40 and 2.41 in case of a perpendicular field. To acquire the data, some steps must be done to do the standard problem and have some parameters to compare:

Figure 8 – (a) Magnetization varying in time for Ni solid squared pillar and his (b) FFT curve.



Source: Elaborated by the author (2021)

- The initial magnetization configuration is obtained in the relaxation stage by simulating the standard problem (BAKER et al., 2017). The relaxation stage is used to bring the system into a precise. Starting from an initial uniform magnetization in the direction perpendicular to the principal axis, the system moves to a “relaxed” state in an attempt to reach a (local) energy minimum due to the high value of the damping coefficient. The relaxed state is used as the initial configuration for the dynamical stage. This process is used in all the geometry which is divided and each cell responds to the LLG equation (Figure 9), paying attention that each cell has a size smaller than the material exchange length. In general, the exchange length, Equation 2.42, is the important scale when the dipolar magnetostatic interaction dominates over the magnetocrystalline anisotropy (FREI; SHTRIKMAN; TREVES, 1957), which is the case of soft magnetic materials (ABO et al., 2013).

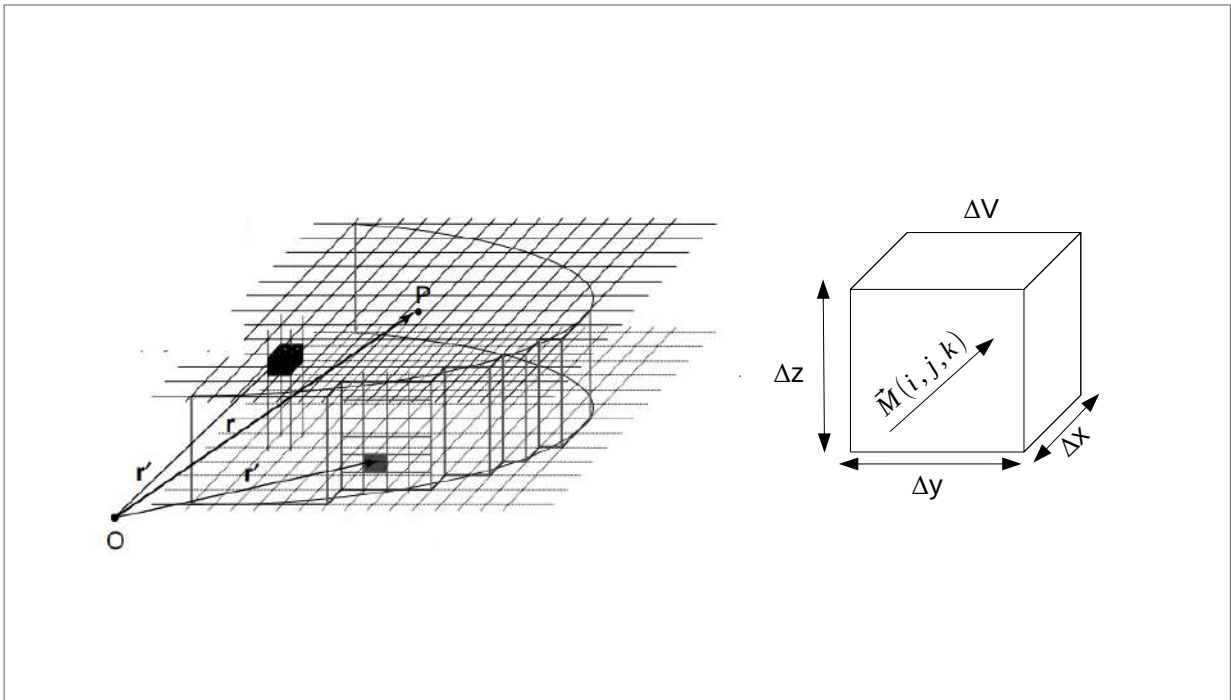
$$l_{ex} = \sqrt{\frac{2A}{\mu_0 M_S^2}}. \quad (2.42)$$

- Besides being reproducible, the field must be sufficiently large to disturb the magnetization dynamics, but small enough so the system remains in the linear regime. This is achieved by changing the direction of the bias field, as a simple practical approach that does not require time-dependent applied fields. Foreseen that most of the simulations

tools, even the ones that do not support varying time external fields, are able to excite the system in this manner because the stages of magnetization (relaxation and dynamic) have the information of the variation in time.

- Computation time: In micromagnetic simulations, the computational time depends mainly on the number of cells in the discretized problem, which depends on the mesh size, geometry, and the adopted procedure to magnetization dynamic evolution (Evolver).
- Verification of results: Ideally, results should be verified against other methods of obtaining them. In this work, the results are verified with the paper (BAKER et al., 2017) that guarantees us confidence in the outcome.

Figure 9 – Representation of discretization of a magnetic sample in a mesh of individual cells of volume $\Delta V = \Delta x \Delta y \Delta z$ (left). Each cell has uniform magnetization \vec{M} (right).



Source: KRONMÜLLER; PARKIN (2007)

2.3 SHAPE ANISOTROPY IN MAGNETIC STRUCTURES

In this section, we study how the shape anisotropy field works for different structures. As Kools *et al.* and Yalccin *et al.* already explained, the anisotropy field is a hypothetical field capable to align the magnetization perpendicular to the easy axis (KOOLS; MOREL, 2004; YALÇIN, 2013). For different structures, the shape anisotropy field can be calculated differently

from the procedure in Section 2.2. Investigations done by Encinas-Oropesa *et al.* showed that H_A can be written as (ENCINAS-OROPESA *et al.*, 2001):

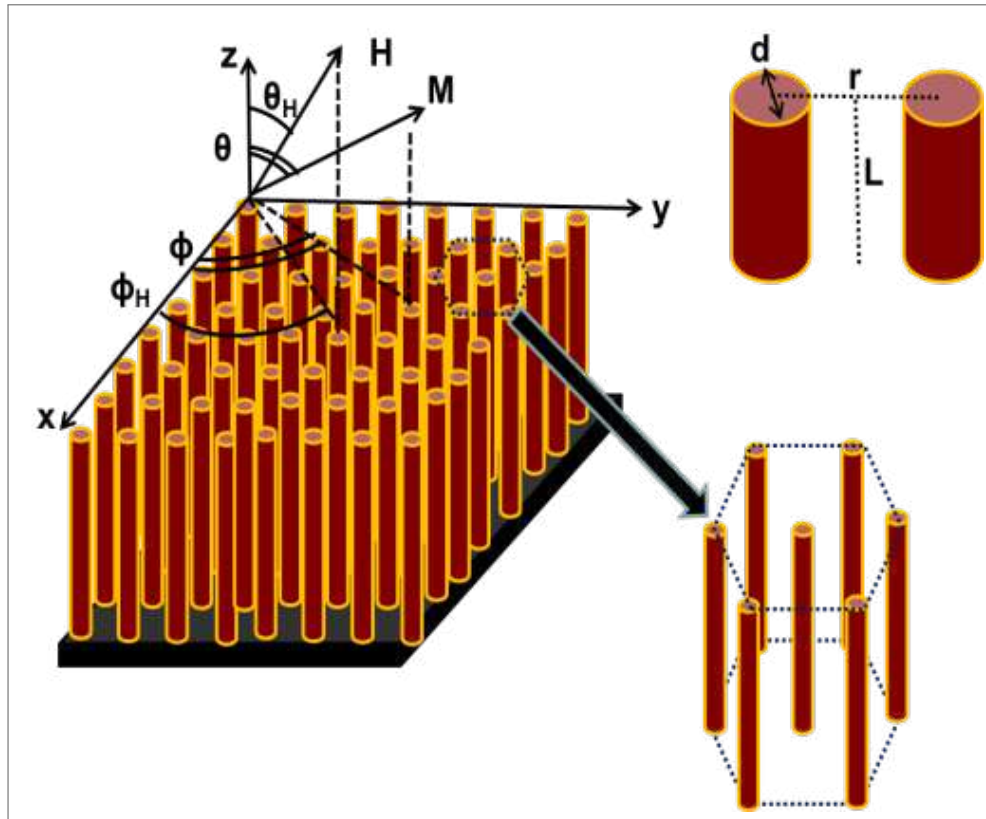
$$H_A = 2\pi M_S(1 - 3P) \text{ in (Centimetre-Gram-Second system of units (CGS)),} \quad (2.43)$$

where P represents packing factor, which can be defined as:

$$P = \frac{\text{Area of array component}}{\text{Area of array region}}$$

According to Encinas-Oropesa *et al.*, the Equation 2.43 reaches the limit of singular nanowire when $P \rightarrow 0$ and when the array approaches to the point of looking like a continuous film $P \rightarrow 1$ (ENCINAS-OROPESA *et al.*, 2001). The same authors have taken into consideration the dependence of the magnetic properties on the packing factor P . For $P < \frac{1}{3}$, the system presents a unidirectional magnetic anisotropy (parallel to the wire axis) changing to the easy plane magnetic anisotropy (perpendicular to the wires) for $P > \frac{1}{3}$.

Figure 10 – Coordinate system for an array of nanowires.



Source: YALÇIN (2013)

Looking Figure 10 and using the definition of the packing factor, it can be easily used the area of one triangular region of the hexagonal array which is $A_{region} = \frac{\sqrt{3}r^2}{4}$ where $\frac{\sqrt{3}}{4}$ comes

out from one side of the equilateral triangle formed by 3 pillars (YALÇIN, 2013). After using all these principles, it can be found:

$$P = \frac{\pi d^2}{2\sqrt{3}r^2}. \quad (2.44)$$

In this work, we simulate the squared NPs array. Examining this system, because of different geometry, it is not possible to use Equations 2.43 and 2.44. It is necessary to find another relation for the packing factor. For generic kind of structure, the adopted procedure was related by Hernandez *et al.* by using the generalized equation (HERNÁNDEZ; REZENDE; AZEVEDO, 2008):

$$H_A = 2\pi M_S(\alpha - \beta P) \text{ in (CGS)}. \quad (2.45)$$

In Equation 2.45, α and β are phenomenological constants that can be determined for any structure by graphical adjustment. For the NPs array the area can be simplified because of its geometry and it can be used to determine the constants of Equation 2.45:

$$P = \frac{D^2}{a^2}, \quad (2.46)$$

$$P^* = \frac{(D - d)^2}{a^2}, \quad (2.47)$$

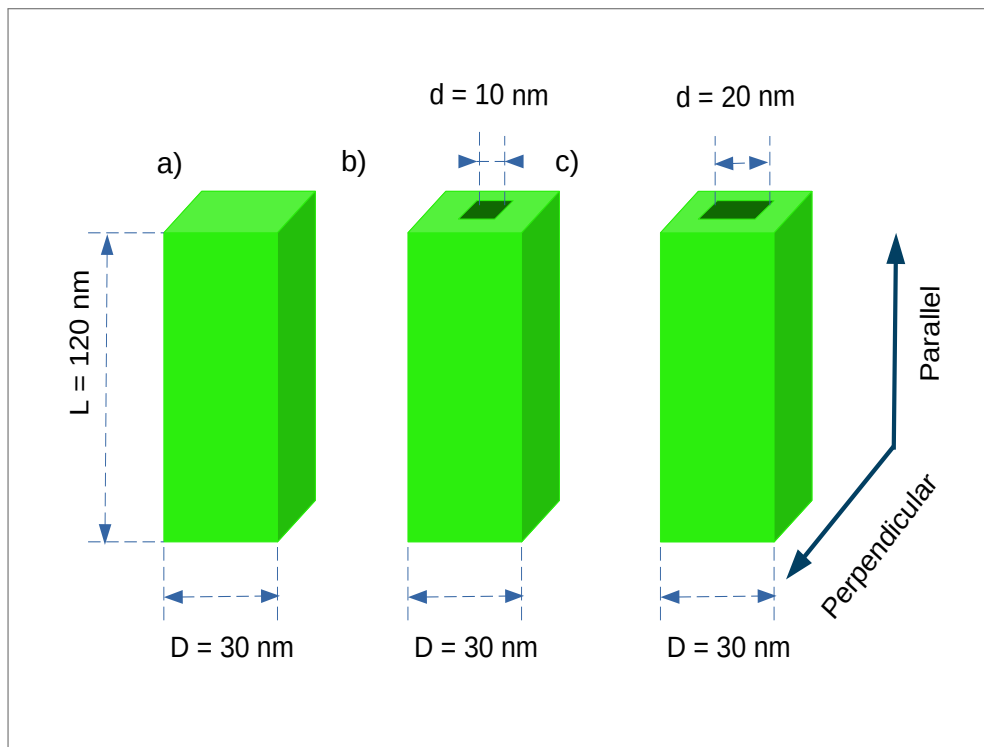
where Equation 2.46 is used to analyze the influence of squared NPs doesn't taking into account the hollowed space, in Equation 2.47 the hollowed space are considered. For these two models, there are some differences to be observed. Considering solid pillar array, there is dipolar interaction between each squared NP's. When the hollow space is considered more dipolar interaction are added due to the inner edges.

For the pillar array systems, D represents the side distance of one squared pillar and a represents the center to center distance in Equation 2.46 this distance is described in the literature as very important because it alters the magnetic response of the system, due to the alteration of the packing factor P (FUENTES *et al.*, 2017). The only difference for Equation 2.47 is that it takes into account the effects of the hole in structure centers. As it can be seen in literature, in this kind of structure, a hole in the center changes the magnetization dynamics (GUERRA *et al.*, 2021). In our approximation using Equation 2.45 $\alpha \neq 1$ due to the pillar height L are not much bigger than D . In our studies, $L = 120 \text{ nm}$ and $D = 30 \text{ nm}$.

3 METHODOLOGY

The methodology, was based on Baker *et al* procedure for standard model simulation of FMR (BAKER *et al.*, 2017), which was described in Section 2.2.1. In this dissertation, different types of squared NPs with greater axis length were considered $L = 120$ nm. The analysis starting point was considering the isolated kind with side dimension of 30 nm. This singular NP was simulated with no cavity, see Figure 11a), hollowed with 10 nm, see Figure 11b), and 20 nm, see Figure 11c), in this work (SILVA; GUERRA; PADRÓN-HERNÁNDEZ, 2021).

Figure 11 – Definition of NPs a) solid and hollow with b) $d = 10$ nm and c) $d = 20$ nm.

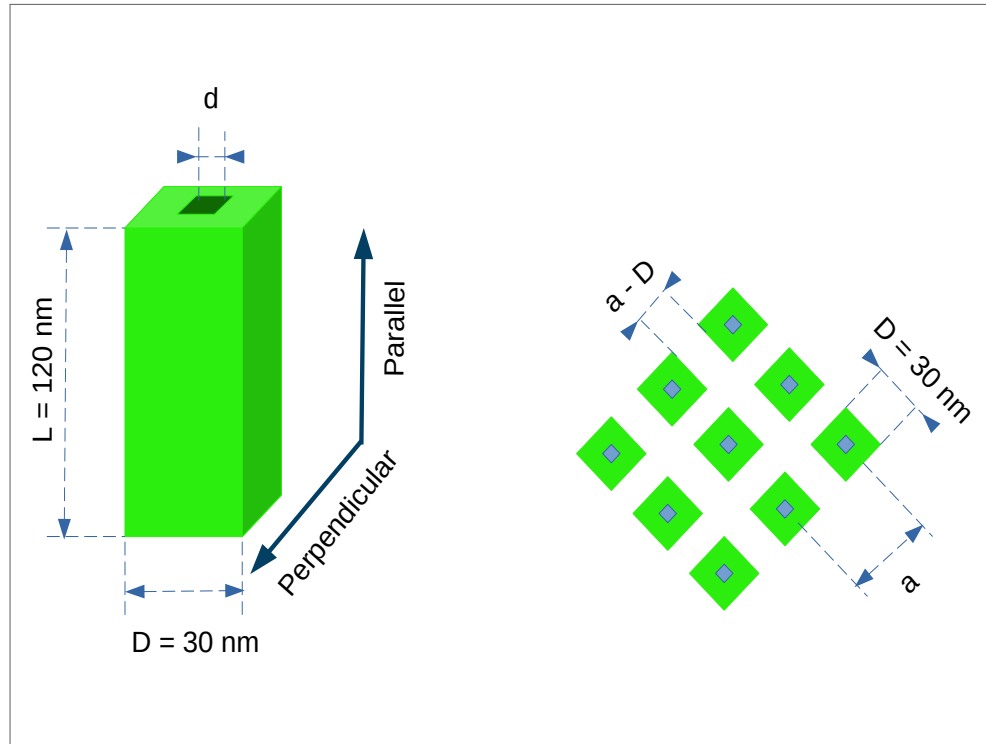


Source: SILVA; GUERRA; PADRÓN-HERNÁNDEZ (2021)

After the isolated NP, the next step was to simulate nanopillar arrays. The simulation was done varying its cavity, as done in the previous example (Figure 11), but now varying either the distance between each pillar (Figure 12), which changed the dipolar interaction.

In all the FMR simulations, the parameters were: $\gamma = 2.211 \times 10^5 \text{ mA}^{-1}\text{s}^{-1}$ and $\alpha = 1$ in the equilibrium condition and $\alpha = 0.008$ in the dynamical phase. These parameters can be found from Equation 2.11. The material chosen for the procedures was Nickel because it has a small magnetocrystalline anisotropy. Thus, the magnetic response must be dominated by the shape anisotropy (EAGLETON; SEARSON, 2004). In this case, the saturation magnetization

Figure 12 – Geometry of 3x3 nanopillar array.



Source: Elaborated by the author (2021)

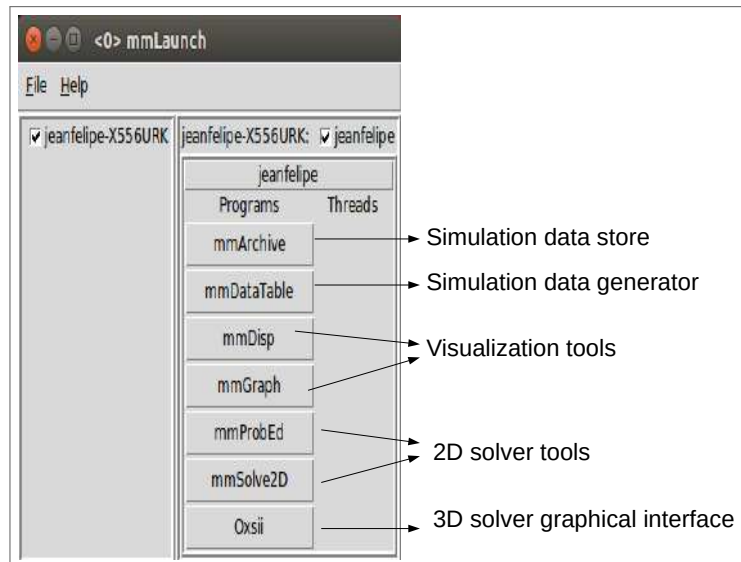
is $M_S = 490$ kA/m, and for the exchange stiffness constant, $A = 9 \times 10^{-12}$ J/m. The volume of each cubic cell from the mesh was $5 \times 5 \times 5$ nm³, so each edge of the cell is 5 nm, which is less than the value of Ni exchange length $l_{ex} \approx 7.72$ nm. This value can be calculated using Equation 2.47.

The system came to energetic equilibrium under a static magnetic field acting, with $\alpha = 1$. During the relaxation process, the field applied had an angle of 88.8° in the y-direction. This process remained for 5 ns, then the dynamic process was started, with $\alpha = 0.008$ and an angle of 90° for the rest of the simulation (20 ns). The external field was applied from 20 to 400 kA/m and every magnetic response was recorded in an OpenDocument Text File format (ODT) file and later post-processed by using FFT and fit adjustments based on Encinas-Oropesa *et al* (ENCINAS-OROPESA *et al.*, 2001). To calculate all the simulation in the present work it was used a Central Processing Unit (CPU) Intel(R) Core(TM) i5-7200U CPU @ 2.50 GHz with 8 GB of RAM.

3.1 OBJECT ORIENTED MICROMAGNETIC FRAMEWORK (OOMMF)

The OOMMF package, is a micromagnetic simulator developed by National Institute of Standards and Technology (NIST) (DONAHUE; DONAHUE, 1999). Its code, was written in C++ (STROUSTRUP, 2000) and TCL/TK (OUSTERHOUT; JONES, 2009). It can be used in many Operational System (OS) such as: Unix, Windows NT (64 bits) and Windows 9x (32 bits). It was not structured in a single program, but a collection that are useful depending on the simulation applicability. Each program works in specified tasks as part of a micromagnetic simulation system and can be chosen in Graphical User Interface (GUI) or by specific commands using the Terminal.

Figure 13 – OOMMF Graphical User Interface launcher.



Source: Elaborated by the author (2021)

An advantage of this modular architecture is that each program can be improved or replaced without having to redesign the system as a whole. The Oxs tool is mainly written in C++ and the other tools besides GUI are written in TCL/TK. The code can be modified at 3 different levels:

- At the first level, individual programs interact through defined protocols over a network device. They can be connected in different procedures from the user interface GUI, as seen in Figure 13.
- The secondary level of modification is through the use of the TCL/TK script. Some modules allow TCL/TK scripts to be imported and run and high-level scripts are relatively

easy to modify or replace, see Figure 16.

- At the last level, the C++ code itself can be modified as seen in Figures 14 and 15.

Oxs (OOMMF eXtensible Solver) is the extensible micromagnetic calculation engine, efficient of solving problems written in a three-dimensional mesh of rectangular cells that contain the three-dimensional magnetization spin. There are two interfaces assigned to Oxs: the interactive interface (Oxsii), in Figure 13, which can be controlled through a GUI, and the batch mode (Boxsi), which is used via the Terminal command line, which is "apt" for using shell scripts.

The problem definition in Oxs is achieved from input files in ".MIF" format. A simulation in Oxs is done as a collection of Oxs_Ext entry parameters (Oxs extensions). These parameters are defined through specific blocks in the input Memory Initialization File (MIF) file. The Oxs_Ext parameters available in OOMMF can be organized into Atlases, Grids, Energies, Evolvers, Drivers, Scalar Field Objects, Vector Field Objects, and glsMIF Support Classes:

- Atlases: The simulation geometry is specified in Oxs through the atlas, which divides the domain into one or more separated subsets called regions. The available atlas types are Oxs_BoxAtlas, Oxs_ImageAtlas, Oxs_MultiAtlas, Oxs_ScriptAtlas, and Oxs_EllipsoidAtlas. The most used atlas is Oxs_BoxAtlas for simple rectangular geometries. Oxs_ImageAtlas is used to input geometries through images and is limited to the case of two dimensions. In Oxs_ScriptAtlas, the geometry is defined using TCL scripts.
- Meshes: Simulation discretization is defined. There must be only one mesh declared by the MIF file. The only default mesh available is the Oxs_RectangularMesh. This is the reason to call OOMMF of a FDM simulator.
- Energies: In this part, the energy terms of the simulation are defined. Energy terms must be declared separately in a specific block, independently, *i.e.*, those values are not allowed to be declared inside another Oxs_Ext object. The number of energy terms that can be declared within a MIF file is unlimited. In OOMMF, Magnetocrystalline Energy, Exchange Energy, Magnetostatic Energy, and Zeeman Energy terms are available.
- Evolvers: They are responsible for updating the magnetization configuration from one iteration to the next. There are two types of Evolvers; Time evolvers, to study the dynamics of LLG equation, and minimization evolvers, which locate local minima on

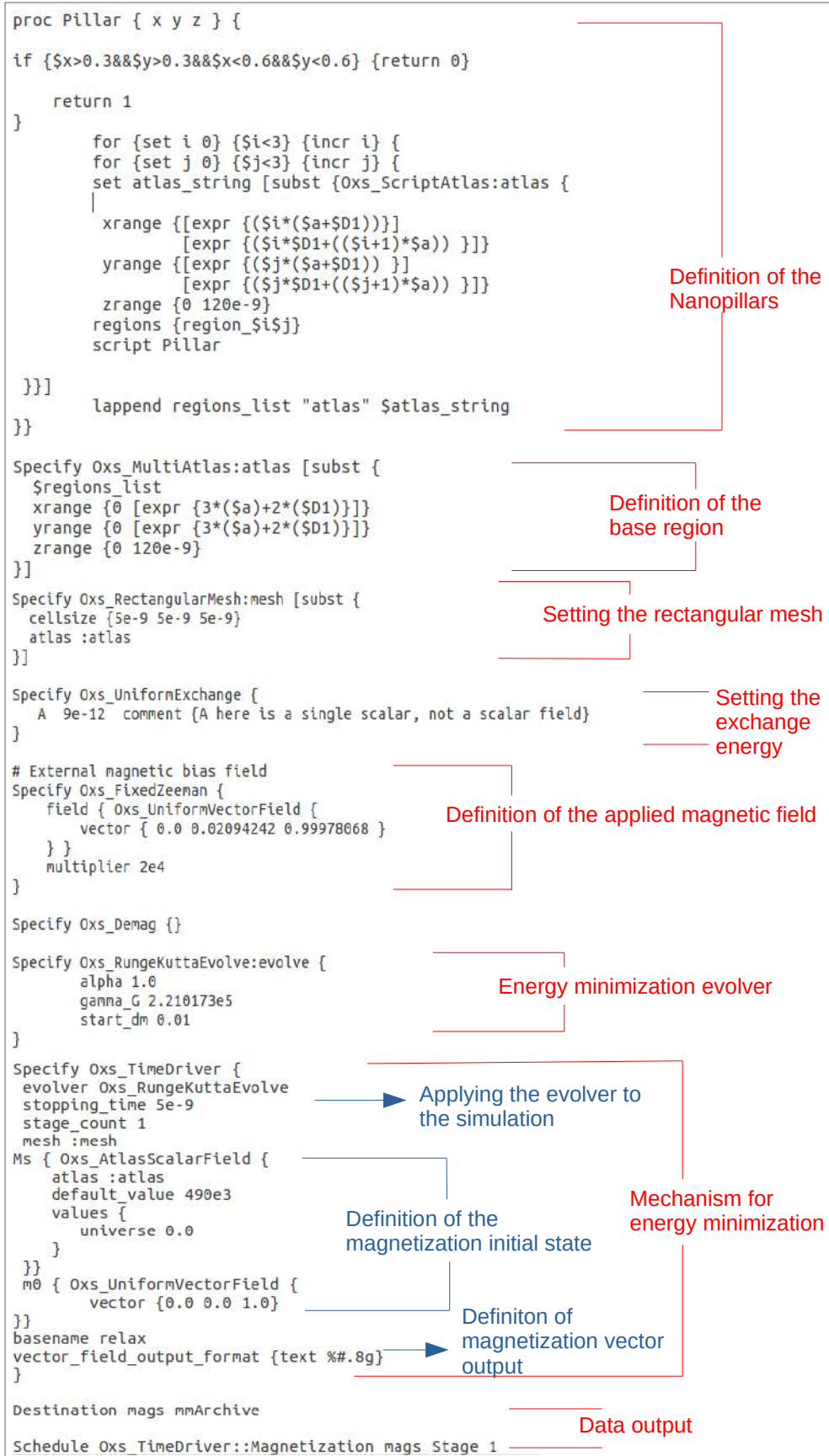
the energy surface using straight-line minimization techniques. Evolvers are controlled by Drivers and must match the appropriate Driver type, *e.g.* Weather Evolvers must be linked with Weather Drivers.

- Drivers: It was seen that Evolvers moves the simulation in individual steps forwardly, the Drivers coordinate Evolver's action in the simulation entirely, by grouping the iterations into tasks, steps, and runs. Tasks are the first level of iterations completed without influencing the user interface response. Steps are made after one cell interacts with the neighbor in the mesh governed by the gIsLLG equation described in the MIF archive; in particular, there is no anticipation for the problem parameters to change discontinuously within a step. The run is the succession of all stages in the problem. The Drivers detect when stages and runs end, taking considering the criteria defined in the problem description in the MIF. In Oxs there are two types of Drivers, Time Drivers, and Minimization Drivers.
- Field Objects return values (scalar or vector) as a function of position. These are often used as objects within specific blocks of other Oxs_Ext objects. They are used to initialize spatially variable quantities, acting like degree material parameters being initial magnetization settings.
- Support Classes for MIF: There is the Oxs_LabelValue object. The string for a specific block of Oxs_LabelValue objects is an arbitrary TCL/TK list of element pairs. The first element of each pair is interpreted as a label, the second as the value. You can use, for example, an Oxs_LabelValue object to keep common values in any block of an Oxs_Ext in different files.

3.1.1 Micromagnetic simulation code

The FMR simulations were generated from the codes below, which are second level, they are defined from a script based on TCL/TK. For the simulation to each field, we use cycles using the Evolver and the minimization driver Figure 14. A simulation of the magnetization dynamics was also carried out using the Evolver and Time Driver. In Figure 14, the simulation for a single Nanopillar or an array of NPs is chosen by setting *i* and *j* to be lesser than one, lesser than two for a 2x2 array, and lesser than three for a 3x3 NPs array. This sample was

Figure 14 – Fragment of nickel nanopillar simulation code in static regime.



Source: Elaborated by the author (2021)

Figure 15 – Fragment of nickel nanopillar simulation code in dynamic regime.

```

Specify Oxs_FixedZeeman {
  field { Oxs_UniformVectorField {
    vector { 0.0 0.0 1.0 }
  } }
  multiplier 2e4
}

Specify Oxs_Demag {}

Specify Oxs_RungeKuttaEvolve:evolve {
  alpha 0.008
  gamma_G 2.210173e5
}

Specify Oxs_TimeDriver {
  evolver Oxs_RungeKuttaEvolve
  stopping_time 5e-12
  mesh :mesh
  stage_count 4000
  Ms { Oxs_AtlasScalarField {
    atlas :atlas
    default_value 490e3
    values {
      universe 0.0
    }
  }}
  m0 { Oxs_FileVectorField {
    file relax.omf
    atlas :atlas
  } }
  basename dynamic
  vector_field_output_format {text %#.8g}
}

Destination table mmArchive
Destination mags mmArchive

Schedule DataTable table Stage 1
Schedule Oxs_TimeDriver::Spin mags Stage 1

```

The field is applied in a different orientation

The damping factor is lower for dynamic stage

The simulation still working in the system for 20 ns

Saturation magnetization of the system

Initial magnetization (received from the static simulation)

Output data

Source: Elaborated by the author (2021)

simulated for the parallel case. To simulate the perpendicular example, it must transfer all the data from xrange to zrange inside Oxs_Multiatlas and vice-versa in the geometry definition and base region.

In Figure 15, there are some aspects to compare from Figure 14. From the beginning, the field is now aligned with the easy axis. The second change is that the damping factor α is reduced to obtain the dynamic stage. The third alteration is to change the time because dynamic simulation remains for 20 ns and receives the first stage from the end of the static simulation. After that, it is necessary to save the output data to find all the further values of interest.

3.2 FMR SIMULATION ITINERARY

All the simulations are performed using a bash script command, after setting up the OOMMF code (Figure 14 and 15), the OOMMF package does not support two codes running

at the same time because after a code run in Boxsi all data is deleted, so it is required to use the two codes from Subsection 3.1.1 in a script, as seen in Figure 16.

3.2.1 Bash Script to execute static and dynamic codes in sequence

This script (Figure 16) was run in Linux terminal. The OOMMF codes and the script were in the same folder and the results were generated in one subfolder. When starting to run the simulation, it generates the number of cells which will be calculated for the magnetization. Computational time is proportional to the number of cells as seen in Table 2 the cavities do not eliminate the computation of each cell inside the cavity, so the hollowed structures have the same time to compute as the solid ones. The only thing that changes the number of cells is the change in the inter-pillar distance as it can be seen in Table 3.

Table 2 – Number of Cells for a Single Pillar

Single Pillar	Number of cells	Spatial arrangement of cells
Solid	864	6 × 6 × 24 cells
10 nm Hollow	864	6 × 6 × 24 cells
20 nm Hollow	864	6 × 6 × 24 cells

Source: Elaborated by the author (2021)

Table 3 – Number of Cells for a Pillar Array

Pillar Array	
Interpillar Distance	Sollid, 10 nm and 20 nm Hollow
5 nm	9600 cells arranged in 20 × 20 × 24 format
10 nm	11616 cells arranged in 22 × 22 × 24 format
20 nm	16224 cells arranged in 26 × 26 × 24 format
50 nm	34656 cells arranged in 38 × 38 × 24 format

Source: Elaborated by the author (2021)

Figure 16 – Fragment of FMR script simulation

```

set -o errexit
OOMMF_SCRIPTS="estatico.mif dinamico.mif postprocessing.py"
echo "Data will be generated in output directory: '$OUTPUT_DIR'"
TMPDIR=$(mktemp -d)
for FILENAME in $OOMMF_SCRIPTS; do
    cp ./FILENAME $TMPDIR/$FILENAME;
done

#
# Change into the temporary directory and run all subsequent commands there.
#
pushd $TMPDIR
echo "Working in temporary directory '$TMPDIR'."
echo "If something goes wrong you may want to delete this manually."

#
# Generate a README.txt file to inform the user how the data in this
# directory was created.
#
TIMESTAMP=$(date)
echo "Generating OOMMF data... This may take a while."

#
# Run the relaxation stage.
#
tclsh /$HOME/oommf/oommf.tcl boxsi +fg estatico.mif -exitondone 1
mv relax-*omf relax.omf

#
# Run the dynamic stage.
#
tclsh /$HOME/oommf/oommf.tcl boxsi +fg dinamico.mif -exitondone 1

#
# Extract the columns for time, mx, my, mz and store them in the file "dynamic_txyz.txt".
#
tclsh /$HOME/oommf/oommf.tcl odtcols < "dynamic.odt" 18 14 15 16 > "dynamic_txyz.txt"

```

Static and dynamic archive are opened simultaneously

The script runs the static simulation first

Then uses the static simulation data as the initial parameters of the dynamic simulation

Saves t, m_x , m_y and m_z

Source: Elaborated by the author (2021)

Reading Figure 16, it can be seen that the relaxation stage (static, $\alpha = 1.0$) is coupled with dynamic stage ($\alpha = 0.008$). The same script was used for the perpendicular and parallel cases and for all NPs kinds.

3.2.2 Post-processing of simulated data

After the script completes all the procedures, It generate a .txt file contains the variables as a function of time, m_x , m_y , and m_z . This archive is essential to carry out the analysis of the magnetization curve x time through an FFT. After doing the transformation for each parallel field into a specific type of structure (e.g. individual solid nanopillar or nanopillar array), the perpendicular field is obtained by performing the same job. After that, it is joined in a file each frequency value for the absorption peaks, see Figure 8b) and make a field x frequency graph. After this step, it is analyzed the saturation magnetization field from which can be determined by H_A . Furthermore, by the (DEMAND et al., 2002) Equations 2.39, 2.40, 2.41, 2.45, 2.46 and

2.47, we can determine other parameters of the unitary nanopillar or nanopillar array.

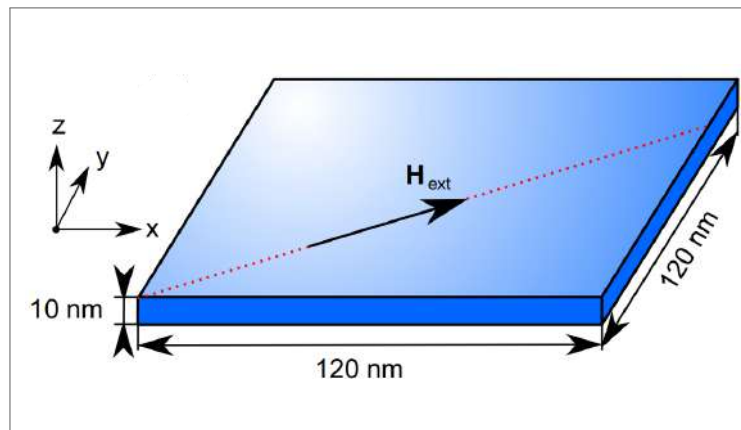
4 RESULTS

The results shown below are based on a comparative analysis of the FMR methodology using the OOMMF for thin films, according to Baker *et al* (BAKER *et al.*, 2017). After understanding that results are similar that of Baker *et al.*, the same analysis is applied to a square nanopillar geometry using different material parameters from the aforementioned paper, because at this point, the material is changed from permalloy to nickel. The nanopillars, as explained in Chapter 3, are built singularly or in arrays and with or without internal cavity of different sizes, in addition to varying the distances between the pillars for the case of arrays.

4.1 THIN FILM

Starting the results by analysing the work described by Baker *et al*. To validate the calculations with those presented by other research groups, the parameters used in the standard problem simulation were repeated, including the application field and the magnetic response seen in Figures 18 and 19.

Figure 17 – Thin film geometry and application of \vec{H} field with 35.56° in the steady phase and 35° in dynamic stage with respect to the x-axis.

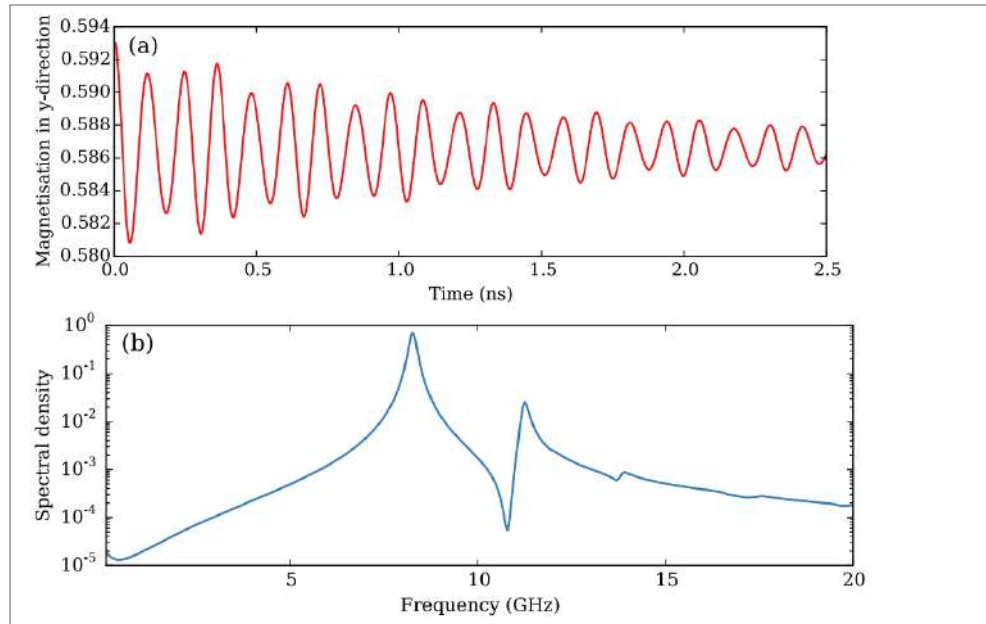


Source: BAKER *et al.* (2017)

The main differences to what was explained at the beginning of the previous chapter, besides the structure (see Figure 17) are the saturation magnetization, which is 800 kA/m for Permalloy (and 490 kA/m for Nickel) and the exchange stiffness constant that has the value of $1.3 \times 10^{-11} \text{ J/m}$. This implies that the sample needs a smaller applied field to saturate when replacing Py by Ni. Furthermore, the reduction of the exchange constant (from 1.3×10^{-11} to

$9 \times 10^{-12} \text{ J/m})$ implies a reduction in the structure interactions.

Figure 18 – a) $m_y(t)$ component of magnetization and b) power spectrum obtained using Fourier transform from the same region.

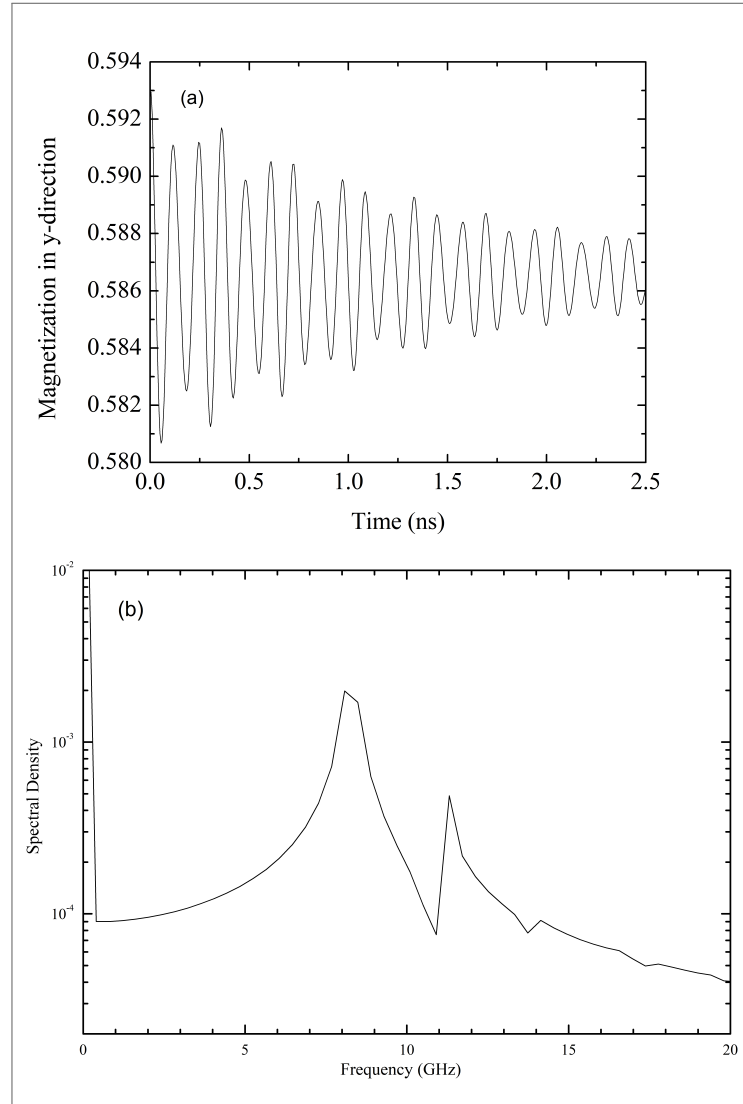


Source: BAKER et al. (2017)

Comparing Figures 18a) and 19a), many similarities in the magnetization behavior can be seen, thus proving the effectiveness of the work initially carried out. However, looking at Figures 18b) and 19b), it is noticed different peak intensities. This refers to the method used by the previously mentioned article (BAKER et al., 2017), which calculates the spectral density smoothed out, where the work carried out in this dissertation was done by calculating only the spectral density by FFT analysis. As the only interest is where the absorption peaks occur, this difference in methodology does not jeopardize what was measured, because, as it can be seen Figures 18b) and 19b) have the primary and secondary peaks in the same position ($\approx 8.5 \text{ GHz}$ and $\approx 11.3 \text{ GHz}$ respectively), which confirms the effectiveness of this work, giving us a yardstick to look back in the problems that will be covered later in this chapter.

In the work of Silva *et al*, was considered different types of squared NPs with $L = 120 \text{ nm}$ (SILVA; GUERRA; PADRÓN-HERNÁNDEZ, 2021). First, they considered the isolated kind with side dimension of 30 nm . These NPs were simulated with no cavity, see Figure 11a), 10 nm hollowed, see Figure 11b) and 20 nm , see Figure 11c) in their cavity.

Figure 19 – Reproduction of thin film (BAKER et al., 2017) a) $M_y(t)$ component of magnetization and b) FFT from the same region.

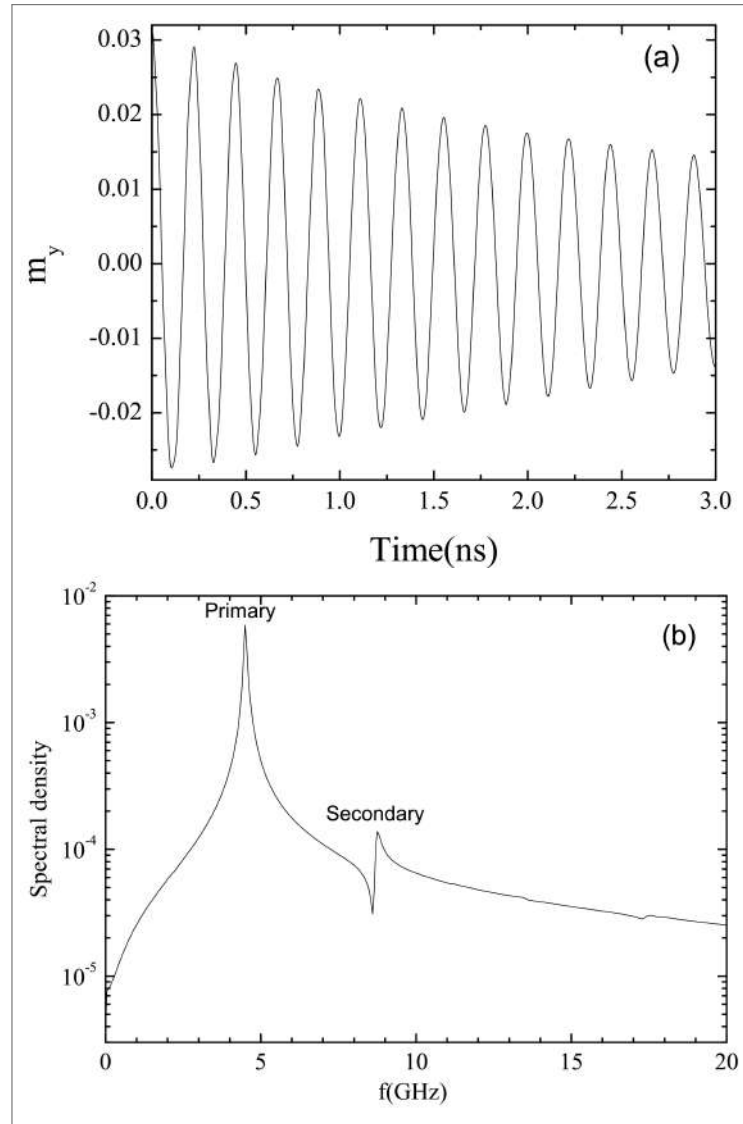


Source: Elaborated by the author (2021)

4.2 ISOLATED NI NANOPILLAR RESULTS

Starting to work with the single nanopillars, see Figure 11, it was performed the entire procedure described in Chapter 3 and generated the magnetization curves as a function of time, subsequently it was calculated the Fourier transform of each curve, as in the example of Figure 20. After got each FFT from parallel and perpendicular situations, as previously described, it was recorded all points of primary peak and secondary peak, see Figure 20b) after the analysis, it was plotted the data of frequency f versus applied field H similar to Figure 7 for both peaks (primary and secondary) to find the shape anisotropy field H_A .

Figure 20 – Isolated nanopillar with $d = 20$ nm a) $m_y(t)$ magnetization component and b) power spectrum obtained using Fourier transform from the same region indicated with primary and secondary peaks with 340 kA/m perpendicular applied field.



Source: Elaborated by the author (2021)

$$\frac{\omega}{\gamma_{\parallel}} = [H_A + H] \quad (4.1)$$

$$\frac{\omega}{\gamma_{\perp}} = \sqrt{H_A^2 - H^2} \quad , H < |H_A| \quad (4.2)$$

$$\frac{\omega}{\gamma_{\perp}} = \sqrt{(H - H_A)H} \quad , H > |H_A| \quad (4.3)$$

Using the Equations 4.1, 4.2, 4.3 as described in literature for nanowires (DEMAND et al., 2002; YALÇIN, 2013) in CGS notation, the results in SI have been already shown in Chapter 2,

equations 4.1, 4.2 and 4.3 looks equal to Equations 2.39, 2.40 and 2.41 because the conversion factor to CGS is implicit in the value of H_A . It can be made a numerical adjustment and get the parameters from those equations. For the adjustment, the theoretical graph shows the behavior of a system with uniaxial anisotropy (Figure 7).

After that, Figure 21a), shows how the frequency varies according to the field, allowing to find the minimum point of this curve, which is where the applied field response of the magnetic moments is minimal, as the frequency approaches zero. In Figure 22a), it was observed a graph similar to the one described above, for the analysis of the frequency variation for the second peak of each applied field. Also, it can be seen in Figure 23 the magnetization hysteresis loop, which is another way to find the H_A , as done by (ENCINAS-OROPESA et al., 2001). In this case, it can be found by looking at the perpendicular remanence point to find the shape anisotropy field.

Comparing all simulation figures for the primary peak, it is found that there are some differences between those and the theoretical graph. In fact, the adjustment does not fit exactly with the theoretical prediction for all the data. This problem gets worse for the secondary peak. Equations 4.1, 4.2 and 4.3 were used in several systems and there are always divergences between the model and the results obtained experimentally and numerically (YALÇIN, 2013; DEMAND et al., 2002).

The divergences most often are due to inhomogeneity of magnetization in very low fields, which lead to the formation of domains. Another possibility is the occurrence of lower-order energetic terms that present symmetry different from the uniaxial one (CHEN; BRUG; GOLDFARB, 1991). Each system has characteristics that depends on the geometry or on greater complexities that can be introduced due to dipolar interactions, as in nanowire arrays in alumina membranes. Working with this experiment, Vázquez *et al* conclude the ratio diameter of nanowires to distance between them is very important to determine the coercivity and remanence values. In fact, both parameters decrease by increasing that ratio as a consequence of the strengthening of the magnetostatic interaction (VÁZQUEZ et al., 2004). Also the Measurements of FMR have allowed them to confirm that arrays with higher ordering present larger non-homogeneity in the diameter of the wires. The effects of changes in the resonance field, due to shape effects, have been frequently reported and for nanometric objects, it has great effects due to the intensity of dipolar interactions (SAAVEDRA et al., 2019; RAPOSO et al., 2016; ZHANG; DIVAN; WANG, 2011; OTÁLORA et al., 2017; LANDEROS; ESCRIG; SALCEDO, 2007).

4.2.1 Solid case for nanopillar

For solid pillar, it can be found from the fitting adjustment of the red lines using Equation 4.1 of Figure 21a) and Figure 22a) that for parallel FMR, $H_A = 97.2$ kA/m, for primary peak and $H_A = 222.5$ kA/m for secondary peak, respectively. Looking for the perpendicular FMR of structure, it is found by adjustment made using Equations 4.2 and 4.3: $H_A = 175$ kA/m, for primary peak and $H_A = 247.5$ kA/m for secondary peak. These can be seen from the blue lines of Figure 21a) and Figure 22a). Comparing to Figure 23a), for the perpendicular case, it is found that the results are equivalent, and the sample gets saturated as it says in the FMR simulation primary peak.

4.2.2 Solid pillar with hole of $d = 10$ nm

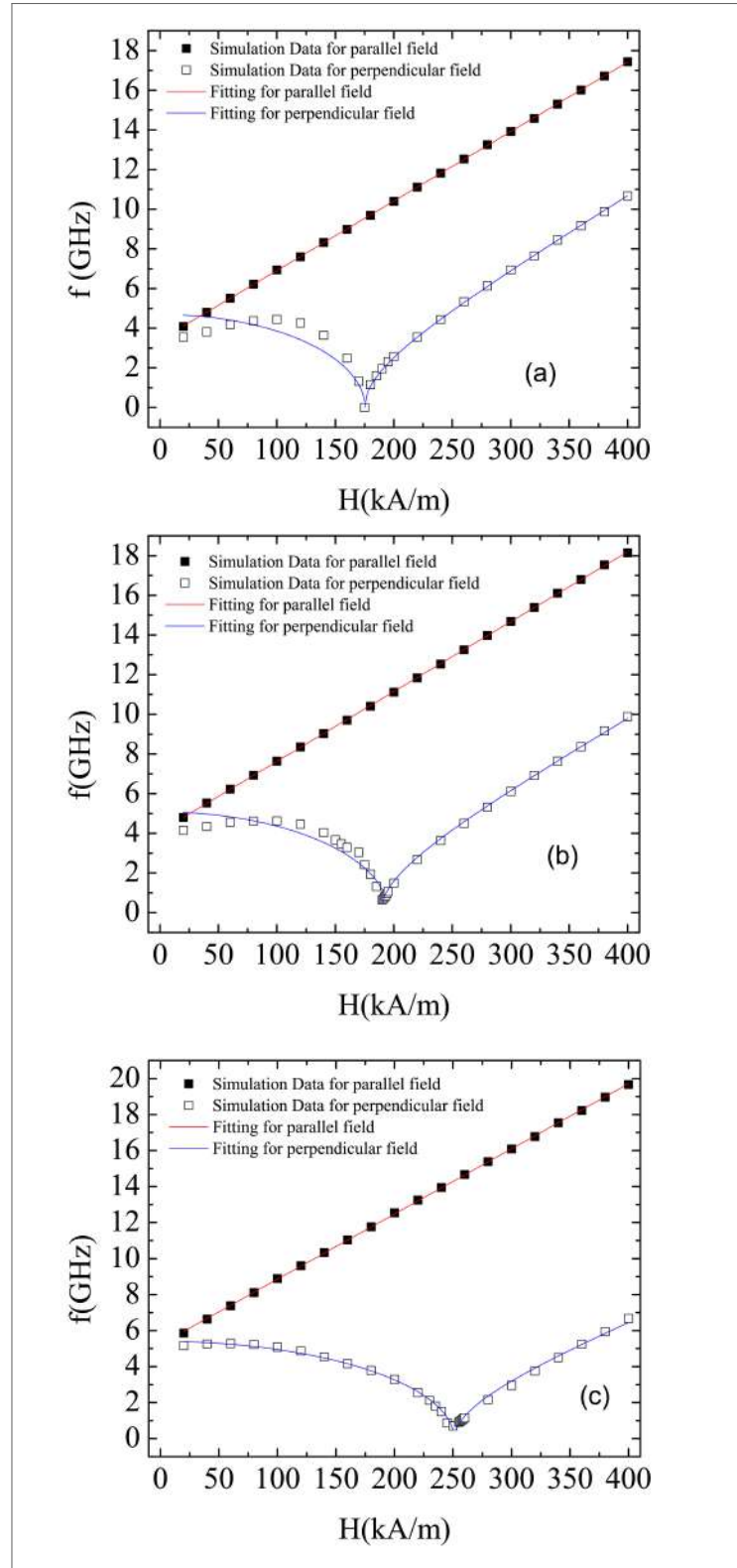
For the pillar with 10 nm hollow, it can be seen that for parallel FMR, $H_A = 116.4$ kA/m, for primary peak and $H_A = 220$ kA/m for secondary peak. It can be seen from the red lines of Figure 21b) and Figure 22b). Looking for the perpendicular FMR of structure, it is found: $H_A = 195$ kA/m, for primary peak and $H_A = 235$ kA/m for secondary peak. It can be seen from the blue lines of Figure 21b) and Figure 22b). Comparing to Figure 23b), for the perpendicular case, it is found that the results are equivalent, and the sample gets saturated as it says in the FMR simulation primary peak.

4.2.3 Solid pillar with hole of $d = 20$ nm

For the pillar with 20 nm hollow, it can be seen that for parallel FMR, $H_A = 144.5$ kA/m, for primary peak and $H_A = 226.9$ kA/m for secondary peak. It can be seen from the red lines of Figure 21c) and Figure 22c). Looking for the perpendicular FMR of structure, it is found: $H_A = 251$ kA/m, for primary peak and $H_A = 219$ kA/m for secondary peak. It can be seen from the blue lines of Figure 21c) and Figure 22c). Compare to Figure 23c), for the perpendicular case, it is found equivalent results and the sample gets saturated as it says in the FMR simulation primary peak (BERTOTTI, 1998).

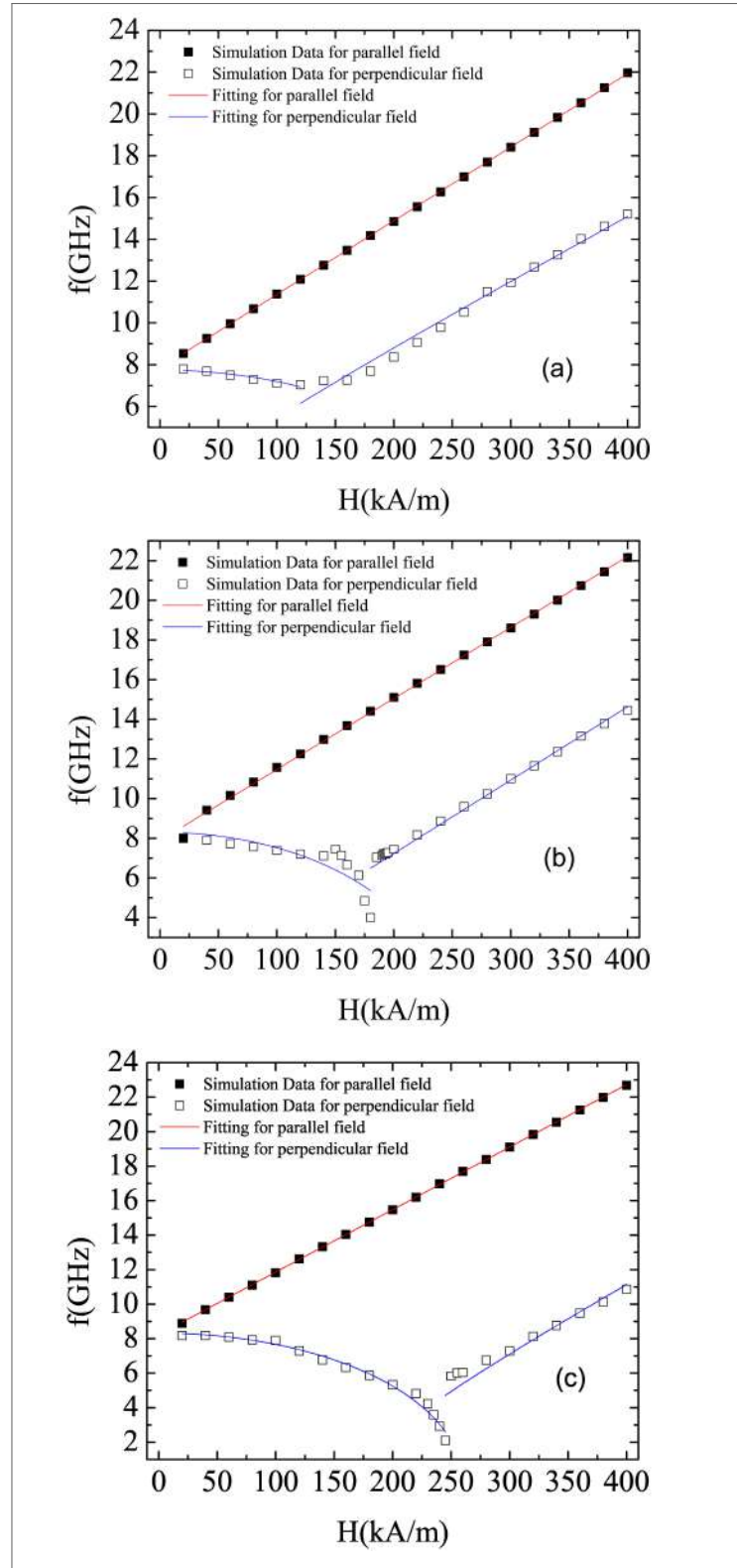
Was mentioned at the beginning of this section that in systems with weak uniaxial anisotropy, there may be divergences in the results in relation to the model of Equations 4.1, 4.2 and 4.3. In the case of square nanopillars, there are several factors that can be responsible for this

Figure 21 – Frequency versus external magnetic field of the main peak at ferromagnetic resonance for isolated:
a) Solid nanopillar (NP) b) hollow NP with 10 nm cavity c) hollow NP with 20 nm cavity.



Source: Elaborated by the author (2021)

Figure 22 – Frequency versus external magnetic field of the secondary peak at ferromagnetic resonance for isolated: a) Solid nanopillar (NP) b) hollow NP with 10 nm cavity c) hollow NP with 20 nm cavity.



Source: Elaborated by the author (2021)

fact because there are divergences due to magnetization inhomogeneity in very low fields, leading to domains formation besides the possible occurrence of lower-order energetic terms presenting different uniaxial symmetry. The saturation magnetization ($M_S = 490$ kA/m) for Ni combined with the low ($L/D = 4$) aspect ratio provide a very low anisotropy field value if originated by shape effects. Furthermore, square geometry with many straight edges offers difficult conditions to saturate the NPs.

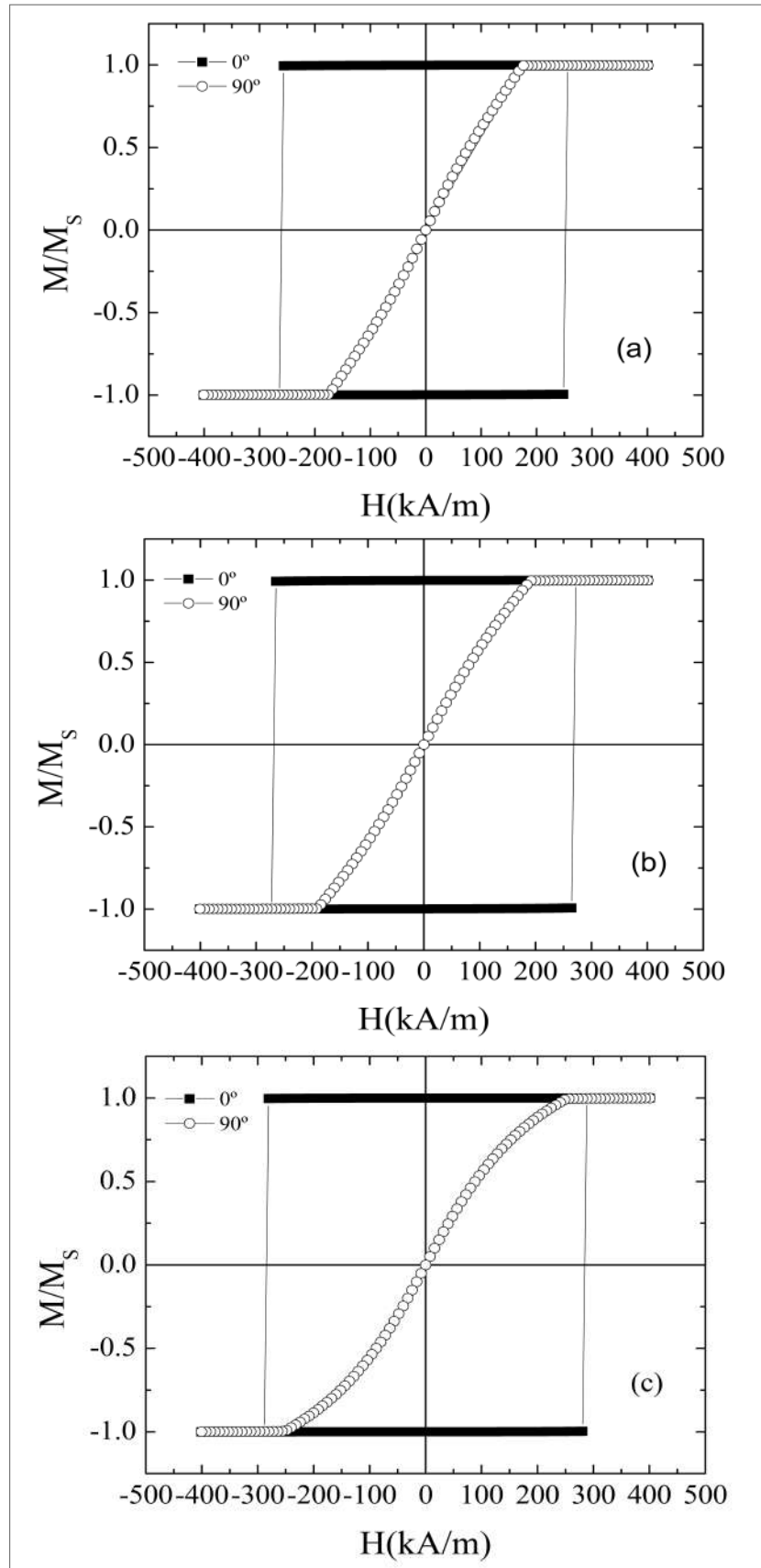
The adjustment with Equations 4.1, 4.2 and 4.3 from referring data of main peak with perpendicular field, Figure 21 (blue line), return values $H_A = 175, 195$ and 251 kA/m, for $d = 0, 10$ and 20 nm, respectively. As the cavity size increases, the adjustment for a smaller field than H_A offers a better fit. This happens because of the increase of anisotropy along the axis of symmetry with d (ZÉLIS et al., 2017). Analyzing referring data from the main peak with the parallel field, Figure 22 (red line), return values of $H_A = 97.2, 116.4$ and 144.5 kA/m, for $d = 0, 10$ and 20 nm, respectively. The increase in d makes closer the internal and external faces of the hollow NPs and for distances of the order of 10 nm, the dipole interactions are significant. In arrays of nickel nanowires deposited on alumina membranes, these inter-wire distances have an order of 20 nm and it is experimentally verified a noteworthy dipole interaction (HUANG et al., 2018; FUENTES et al., 2017).

The model for dipole energy in square pillars with a low aspect ratio between its longitudinal and lateral dimensions presents more corrections. However, this is a system with uniaxial anisotropy in the first order (HERNÁNDEZ, 2009). In this case, uniaxial anisotropy in a perpendicular field leads to larger divergences for all values of d . Thus, it is possible to associate the secondary resonance peak with regions near the corner edges existing in this geometry. Due to this evidence, it was decided to turn attention to the curve that shows the configuration of the parallel field (red line) in Figure 22. Fitting this data with the uniaxial symmetry model (Equations 4.1, 4.2 and 4.3) returns an anisotropy field value that is very close for all d values. The values seen in Subsections 4.2.1, 4.2.2 and 4.2.3 for H_A are $225.5, 220$ and 226.9 respectively.

This significant result shows that the signal from the secondary peak comes from a NP region whose local field does not change with d considerably (HAN et al., 2003). Taking into account the numerical errors from calculations and from fittings the values are constant. A secondary signal was detected in the FMR standard problem paper for thin film geometry; in this case, the secondary signal originates in the corners (BAKER et al., 2017). In nanopillars, the secondary signal has the behavior of a uniaxial contribution according to the curves presented in

Figure 22. The only alternative is a signal coming from the region of the longitudinal (parallel) sharp edges. This secondary peak signal comes from a region whose anisotropy generates weak magnetization along the pillar no mattering the cavity's existence and its size. Moreover, the first signal approximation came from this characteristic is reinforced by having a signal with a perpendicular field which, up to a certain approximation, has the characteristics of the branches of the frequency curve versus field for this type of symmetry (SHARMA; BASU; KUARNR, 2019; ZHANG et al., 2019; JAIMES et al., 2021; HUSSAIN; COTTAM, 2021). The adjustments in Figure 22 shows as the cavity size increases, the uniaxial characteristic of this peak becomes more observable. The reason is that increasing the size of the orifice the inner longitudinal edges move apart. Additionally, the curve in Figure 22a) presents a less strong behavior because in this case, it has only four edges, while for columns with orifice it has eight longitudinal edges.

Figure 23 – Hysteresis cycle for: a) Solid nanopillar (NP). b) Hollow NP with 10 nm cavity. c) Hollow NP with 20 nm cavity.



Source: Elaborated by the author (2021)

4.3 3X3 NI NANOPILLARS ARRAY

Expanding the work, some behaviors of nanopillars array constructed according to the Chapter 3 were also analyzed. This time, changing the internal hole with $d = 0, 10$, and 20 nm, and also the distance from the center of one column to the next, being: $a = 35, 40, 50$, and 80 nm.

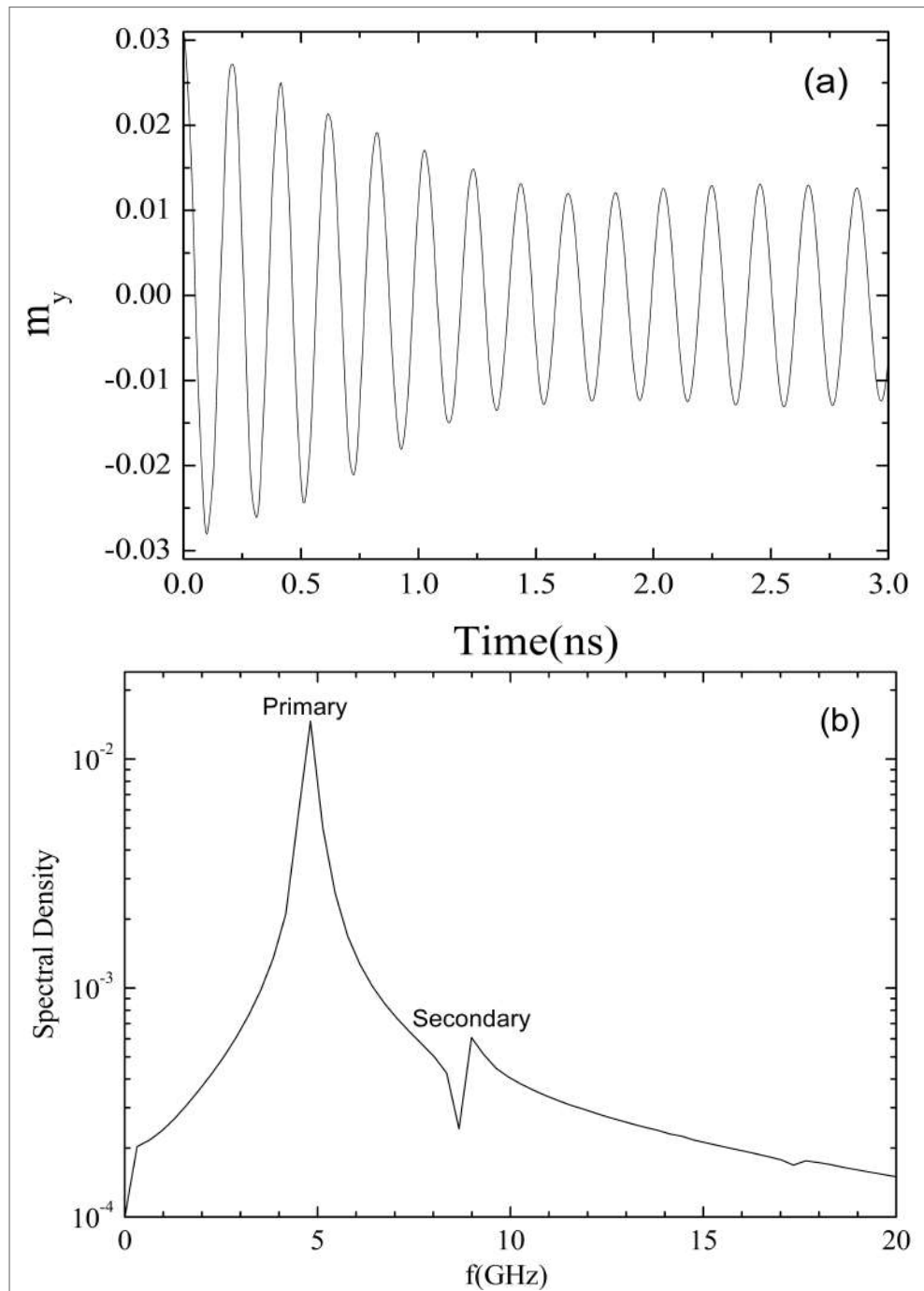
For hollow structures (spherical shell, nanotubes, etc.) a new complexity is inserted due to the magnetic moment confinement (LANDEROS; ESCRIG; SALCEDO, 2007; SALINAS; RESTREPO; IGLESIAS, 2020; ESCRIG et al., 2007). In literature, few works are dealing with the properties of hollow square magnetic nanopillars (NPs). Recently a study about the static magnetic properties of these structures was reported and the cavity effects were found to be significant (GUERRA et al., 2021). Due to the valuable information that dynamic studies offer, specifically FMR, it is of great relevance to have literature analysis on NPs array because it can be used to understand the interactions between neighbors nanopillars. For simplicity, this time the complexity introduced by the cavity in hollow structures and also when they are in arrays a few nanometers apart, this time it will be presented a study by FMR of hollow nickel nanopillars with a square base disposed in an array. The signal was obtained from micromagnetic simulation through a standard problem reported in literature (BAKER et al., 2017).

Observing that results of the secondary peaks in Section 4.2 were not as coherent according to the Equations used (4.1, 4.2 and 4.3), it was decided to observe only the results of the primary peaks in this secondary geometry analysis. At FFT, some small peaks can be observed, but the main one is that it represents the ferromagnetic resonance (main FMR mode), just as measurements performed in laboratories using Electron Paramagnetic Resonance (EPR) equipment (HERNÁNDEZ; REZENDE; AZEVEDO, 2008), where measurements obtained from ferromagnetic nanowire arrays give detailed information on the size of the nanowires. The spectra can be used to calculate the interwire magnetic interactions quite accurately (YALÇIN et al., 2004). Another method to observe the signal of primary resonance peaks is by strip-line using Vector Network Analyzer (VNA) which is an instrument developed for characterization of electrical devices by sending an electromagnetic wave. The transmittance and reflectance are used for FMR experiments. The models of VNA have frequency ranging from 0 to 100 GHz. Thus, it can serve as a microwave bridge to extract FMR parameters at a very broad frequency band (KRAUS et al., 2011; SAAVEDRA et al., 2019; YALÇIN, 2013).

Before the discussion of the results, it is important to recall the behavior of the FMR

frequency with the external magnetic field for a system with uniaxial anisotropy. The theoretical dependence for field parallel to the easy axis is affected by the anisotropy field, H_A , according to Equation 4.1 (YALÇIN, 2013; DEMAND et al., 2002; CHEN; BRUG; GOLDFARB, 1991). For the axis perpendicular field, the dependence is not linear in low fields and there is branching with an intercept at the field H_A , (Equations 4.2 and 4.3) on frequencies.

Figure 24 – Nanopillar array with $d = 20$ nm and $a - D = 50$ nm a) $M_y(t)$ magnetization component and b) FFT showing maxima absorption frequencies from the same region indicated with primary and secondary peaks with 340 kA/m perpendicular field



Source: Elaborated by the author (2021)

These divergences occur because FMR calculations are performed with the assumption of homogeneous magnetization as it can be seen by Equation 2.22. In low external fields, this condition is not met for most systems. Another possibility of deviations from theoretical behavior occurs when the system to be analyzed has other orders of anisotropy that can manifest in certain situations (CHEN; BRUG; GOLDFARB, 1991). One of the possibilities of uniaxial anisotropy is due to the shape of the objects, shape anisotropy. For arrays of nanowires packed in alumina membranes, this effect is predominant, which is combined with an additional term due to interactions between nanowires typically spaced a few nanometers apart (DEMAND et al., 2002; SAAVEDRA et al., 2019; RAPOSO et al., 2016; ZHANG; DIVAN; WANG, 2011; OTÁLORA et al., 2017; LANDEROS; ESCRIG; SALCEDO, 2007).

The studied system in this stage has, in principle, the same behavior as nanowires in alumina membranes. On the other hand, there are two fundamental differences: one due to the square shape of the Ni pillars studied here and the other due to the square arrangement of the sample, different from the hexagonal arrangement of the aforementioned nanowires. Even so, it is possible, in principle, to use the Kittel's equations. As mentioned before, an FMR simulation was conducted in an array of Ni columns with distance $a = 35, 40, 50$, and 80 nm from center to center. There was a cavity in the center of each squared pillar just as proceeded in Section 4.2.

4.3.1 3x3 Ni solid pillar array

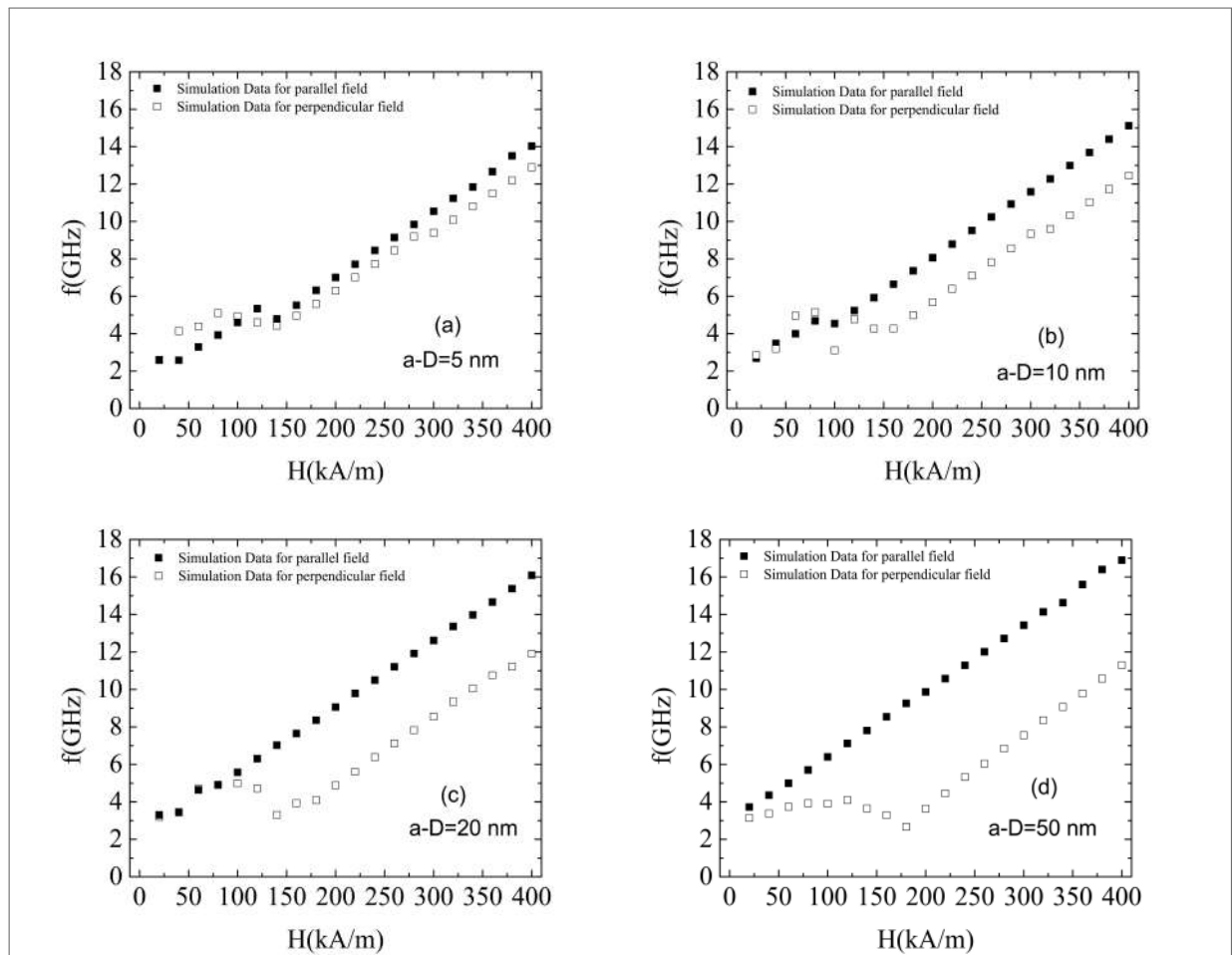
For solid pillar, it can be seen that for parallel FMR, $H_A = 39.07$ kA/m, for $a - D = 5$ nm in Figure 25a) according to the adjustment made from Equation 4.1. Looking for $a - D = 10$ nm parallel FMR of structure, it was found $H_A = 50.98$ kA/m in Figure 25b). For $a - D = 20$ nm parallel FMR of structure, it was detected $H_A = 65.68$ kA/m in Figure 25c) and lastly for $a - D = 50$ nm parallel FMR of structure, it was discovered $H_A = 83.67$ kA/m in Figure 25d).

The width of the pillars was 30 nm and for the longest distance ($a = 80$ nm) it is expected that the effects of the elongated shape of the pillars will manifest, as shown in Figure 25d). The graphs in Figure 25 show the dependence of the resonance frequency with the external field for the arrangement of hollow columns in a perpendicular field and parallel to the central axis of the columns. The curves show how the effects of uniaxial anisotropy decrease as the distance ($a - D$) between the pillars decreases.

The curves in Figure 25a), are confused showing a low uniaxial character for $a - D = 5$ nm. It may also have to do with the fact that structure in Figure 12 for $a - D = 5$ nm and $a - D = 10$ nm has a complete array length of 100 nm and 110 nm respectively as the columns are solid, in this case, it approaches to a situation where there is an isotropic structure, approximately a cube, mainly because the height of the pillars is 120 nm. At this distance, the pillars are very close together and tend to form a compact structure. As $a - D$ increases its value, the nanopillars are increasingly farther apart and the interactions between them diminished, making the predominance of the uniaxial character more evident, Figure 25.

This effect has been observed in nanowires deposited on polycarbonate membranes and also on alumina membranes. In the case of alumina membranes, there is a critical packing value in which the anisotropy is zero and takes place in packing approximately equal to 30% (DEMAND et al., 2002; SAAVEDRA et al., 2019; RAPOSO et al., 2016; ZHANG; DIVAN; WANG, 2011; OTÁLORA et al., 2017; LANDEROS; ESCRIG; SALCEDO, 2007).

Figure 25 – Frequency versus external magnetic field corresponding to a magnetic solid nanopillar array with uni-axial symmetry.



Source: Elaborated by the author (2021)

4.3.2 3x3 Ni hollowed with $d = 10$ nm pillar array

For the pillar with 10 nm hollow, it can be seen that for parallel FMR, $H_A = 46.22$ kA/m, for $a - D = 5$ nm in Figure 26a) according to the adjustment made from Equation 4.1. Looking for $a - D = 10$ nm parallel FMR of structure, it was found $H_A = 66.46$ kA/m in Figure 26b). For $a - D = 20$ nm parallel FMR of structure, it was detected $H_A = 84.57$ kA/m in Figure 26c) and lastly for $a - D = 50$ nm parallel FMR of structure, it was discovered $H_A = 105.97$ kA/m in Figure 26d).

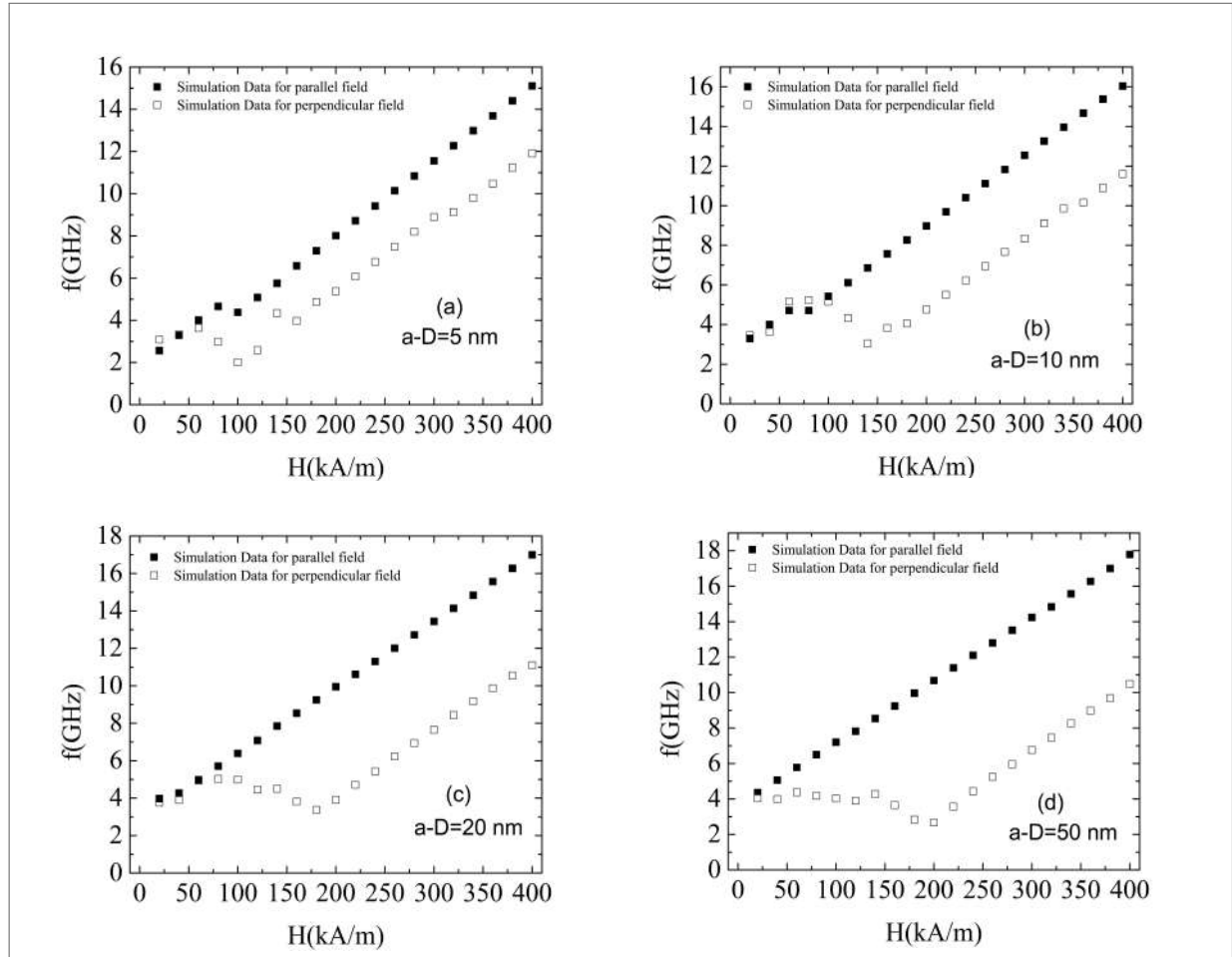
The curves in Figure 26 show the resonance frequency dependence for hollow columns with cavity $d = 10$ nm. Comparing the curves with those shown in Figure 25, it is quite evident that there is an increase in the anisotropy field at all $a - D$ distances studied here. Fits with Equations 4.1, 4.2 and 4.3 were performed on all curves and the anisotropy field obtained values will be discussed very shortly. The cavity effect is shown to be beneficial to increase the anisotropy of the set, thus the columns with $a - D = 80$ nm show a very marked dependence and are comparable with those presented by other studies on cylindrical geometries (DEMAND et al., 2002; SAAVEDRA et al., 2019; RAPOSO et al., 2016).

4.3.3 3x3 Ni hollowed with $d = 20$ nm pillar array

For the pillar with 20 nm hollow, it can be seen that for parallel FMR, $H_A = 94.20$ kA/m, for $a - D = 5$ nm in Figure 27a) according to the adjustment made from Equation 4.1. Looking for $a - D = 10$ nm parallel FMR of structure, it was found $H_A = 108.05$ kA/m in Figure 27b). For $a - D = 20$ nm parallel FMR of structure, it was detected $H_A = 119.57$ kA/m in Figure 27c) and in the last case analyzed for $a - D = 50$ nm parallel FMR of structure, it was discovered $H_A = 134.78$ kA/m in Figure 27d).

In an attempt to make the cavity effects in the columns well established and using the same distances between them in the arrangement, it was used $d = 20$ nm to further enhance the shape anisotropy effects. The curves in Figure 27 shows for all distances $a - D$ a remarkable characteristic behavior of uniaxial anisotropy. Was verified according to the equations mentioned above the fits of this equation with the curves in Figure 25 for solid pillar array ($d = 0$ nm) showing anisotropy fields ranging from $H_A = 39$ kA/m to $H_A = 84$ kA/m as the distance $a - D$ increases from 5 to 50 nm. The increase due to hollow cavity effects with $d = 10$ nm is evidenced by the H_A values from fitting of data corresponding to Figure 26, ranging

Figure 26 – Frequency versus external magnetic field corresponding to a magnetic nanopillar array hollowed with $D = 10$ nm in uniaxial symmetry.



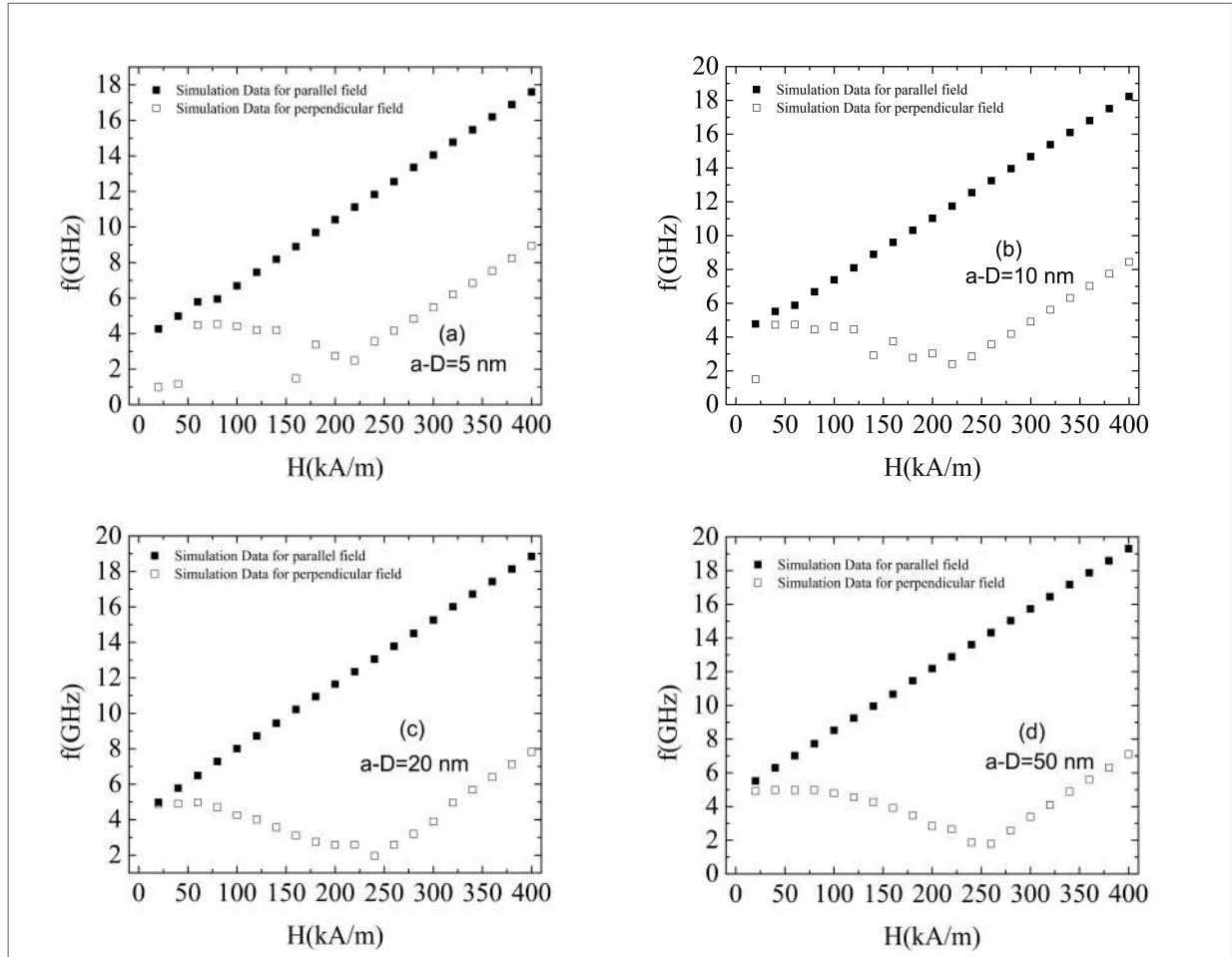
Source: Elaborated by the author (2021)

from 46 kA/m to 106 kA/m for the columns with $a - D = 5 \text{ nm}$ to 50 nm , respectively. The highest values for anisotropy field between 94 kA/m and 135 kA/m were obtained from the curve data fits in Figure 27 in $d = 20 \text{ nm}$ cavity. For comparative purposes, it can be mentioned these values are compatible with those obtained in Ni nanowires with a diameter of 30 nm (HERNÁNDEZ; REZENDE; AZEVEDO, 2008).

In studies with ferromagnetic nanowires, it is very common to use an expression that shows the dependence of the anisotropy field on the distance between the wires when hexagonally packed (LANDEROS; ESCRIG; SALCEDO, 2007). For this specific case, it is common to use $H_A = M_S[1 - 3P]$, where P represents a geometric packing factor that depends on the diameter of the nanowires and the distance between them (ENCINAS-OROPESA et al., 2001).

For the case of square nanopillars presented here, it is pertinent to expect some cause-effect relationship between H_A and d to occur, but it was encountered two typical problems.

Figure 27 – Frequency versus external magnetic field corresponding to a magnetic nanopillar array hollow with $D = 20$ nm in uniaxial symmetry.



Source: Elaborated by the author (2021)

The first, due to the shape of the pillars, which is not ellipsoidal, as used in the model to obtain the ratio of H_A to P . Along with this, it is normal to expect other effects due to the arrangement, in this case, squared, occur. Therefore, it was obtained by evaluating the dependence of the anisotropy field H_A with geometric characteristics that somehow represent the wires packing factor. Specifically, it was decided to use a generic expression proposed in literature (HERNÁNDEZ; REZENDE; AZEVEDO, 2008). In this case, the anisotropy field would be $H_A = M_S[\alpha - \beta P]$, where the value of α comes from the dipole interactions within the columns and β reflects the dipole interactions between the columns of the array.

The next problem in the case of hollow pillars is to understand what the P factor would be actually, because in the case of collecting only the term $P = \frac{D^2}{a^2}$ it is evaluated the filling of the column as a whole, see Figure 12. On the other hand, the real filling factor for the hollow pillars must be estimated with the removal of the cavity volume, *i.e.* $P^* = \frac{(D^2 - d^2)}{a^2}$ in

Figure 12. Because it has an initial study here in which it assesses behaviors, it is used both definitions, as shown in Figure 28 and 29. Those Figures shows the dependence of the H_A anisotropy field with the packaging factor evaluated in the two ways mentioned here to find a better description.

Comparing the two analysis form, it can be made the graphs one below the other in Figure 28 and 29, with Figures 28a) and 29d) for $d = 0$ nm (solid pillars). In them, it can be seen that packing is the same, and the dependence on H_A has the same tendency as it would for nanowires with a negative derivative because the increase in P leads to a critical value at which the anisotropy disappears. The critical value is obtained when $H_A = 0$, which represents an isotropic system. The curves in Figure 28b) and 29e) shows H_A as a function of P and P^* packing for $d = 10$ nm. In them, it only has a change in the derivative of the curves, but compared with the curves for $d = 0$ it is possible to verify an increase in the standard deviation in relation to the straight line.

This deviation (Table 4) is even greater for the curves in Figures 28c) and 29f), where the H_A values are presented as a function of P and P^* for $d = 20$ nm. Even with this gradual increase in deviation, it is possible to verify a good linear behavior of the anisotropy field for both ways of seeing the nanopillar packing. The two forms of analysis lead to relatively different results when fitting the curves. Thus, in order to be able to separate each shape well, it was adjusted the curves $H_A = M_S[\alpha - \beta P]$ for Figures 28a), 28b) and 28c). For Figures 29d), 29e) and 29f), the adjustment coefficients is called by different letters, *i.e.* $H_A = M_S[\alpha^* - \beta^* P^*]$. The results of adjustment can be found in Table 4. These values corroborates with literature results which shows that β^* grows up as critical value decreases (Cavity size increases) (LANDEROS; ESCRIG; SALCEDO, 2007).

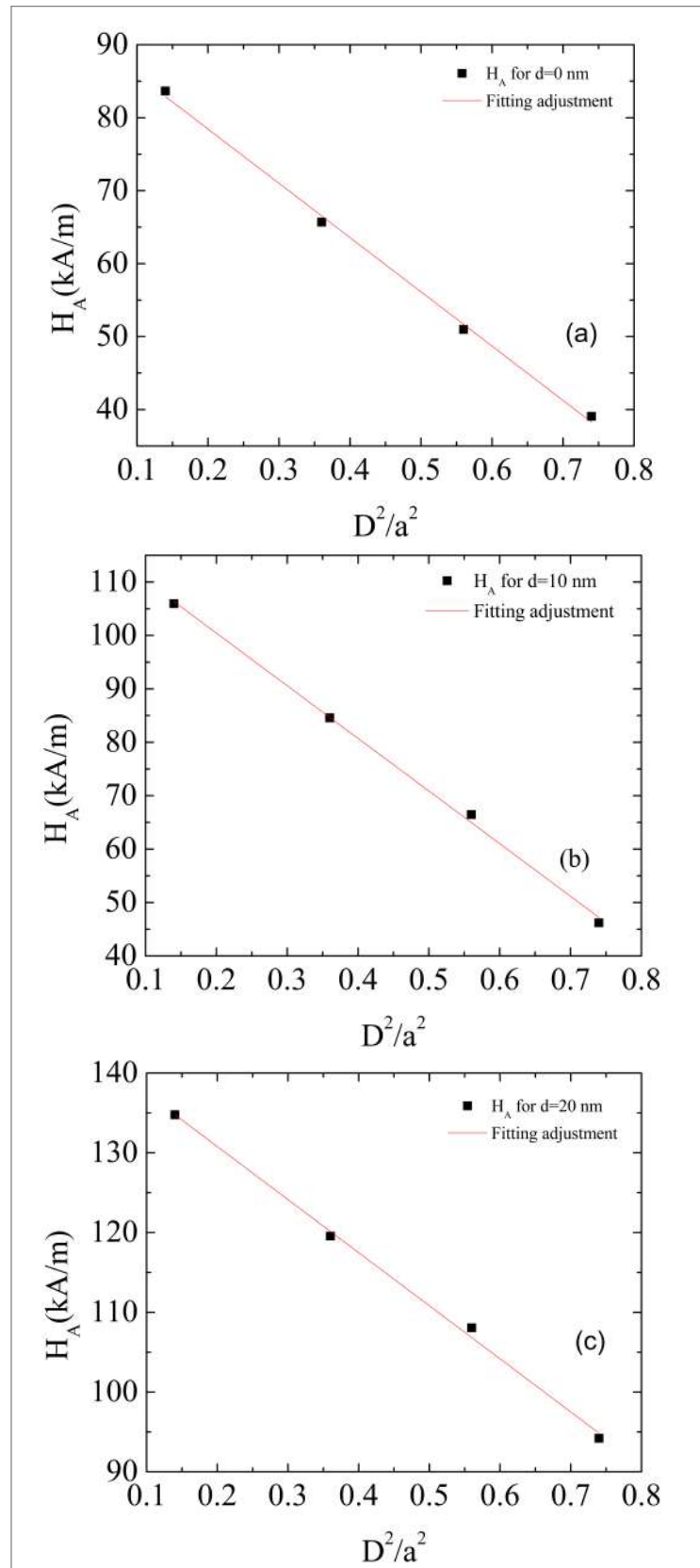
Table 4 – Fitting of adjustment data from Pillar Array as function of d

	α value	α^* value	β value	β^* value
Sollid $d = 0$ nm	0.191 ± 0.002	0.191 ± 0.002	0.152 ± 0.005	0.152 ± 0.005
$d = 10$ nm hollow	0.245 ± 0.003	0.244 ± 0.003	0.200 ± 0.005	0.45 ± 0.01
$d = 20$ nm hollow	0.294 ± 0.002	0.298 ± 0.007	0.140 ± 0.004	1.3 ± 0.1

Source: Elaborated by the author (2021)

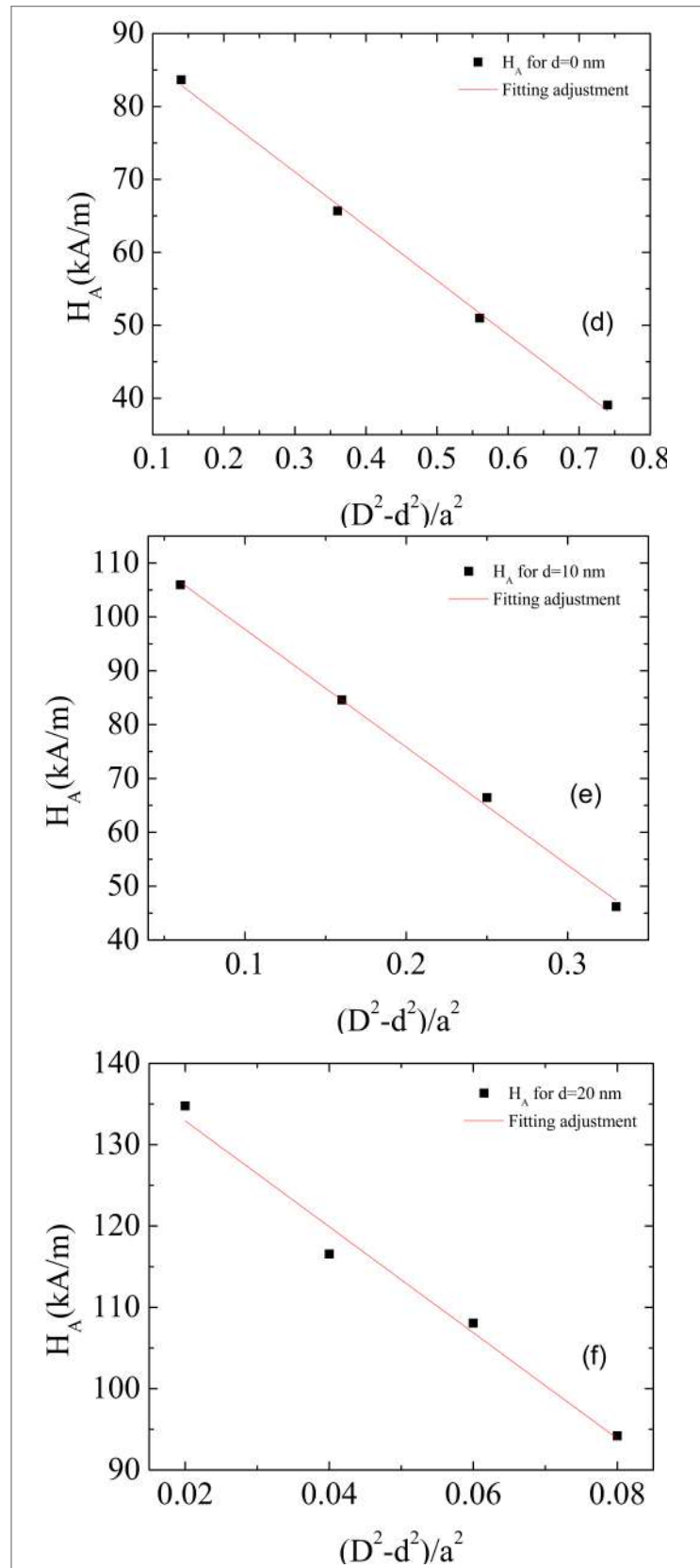
Thus, values of α and $\frac{\alpha}{\beta}$ can be obtained represented in Figure 30a) and 30b) and values for α^* and $\frac{\alpha^*}{\beta^*}$ are shown in Figures 30b) and 30d), all those parameters as a function of the hollow cavity size of the columns. The curves for α and α^* are important because this parameter

Figure 28 – Ni squared nanopillar shape anisotropy field versus packing factor $P = \frac{D^2}{a^2}$



Source: Elaborated by the author (2021)

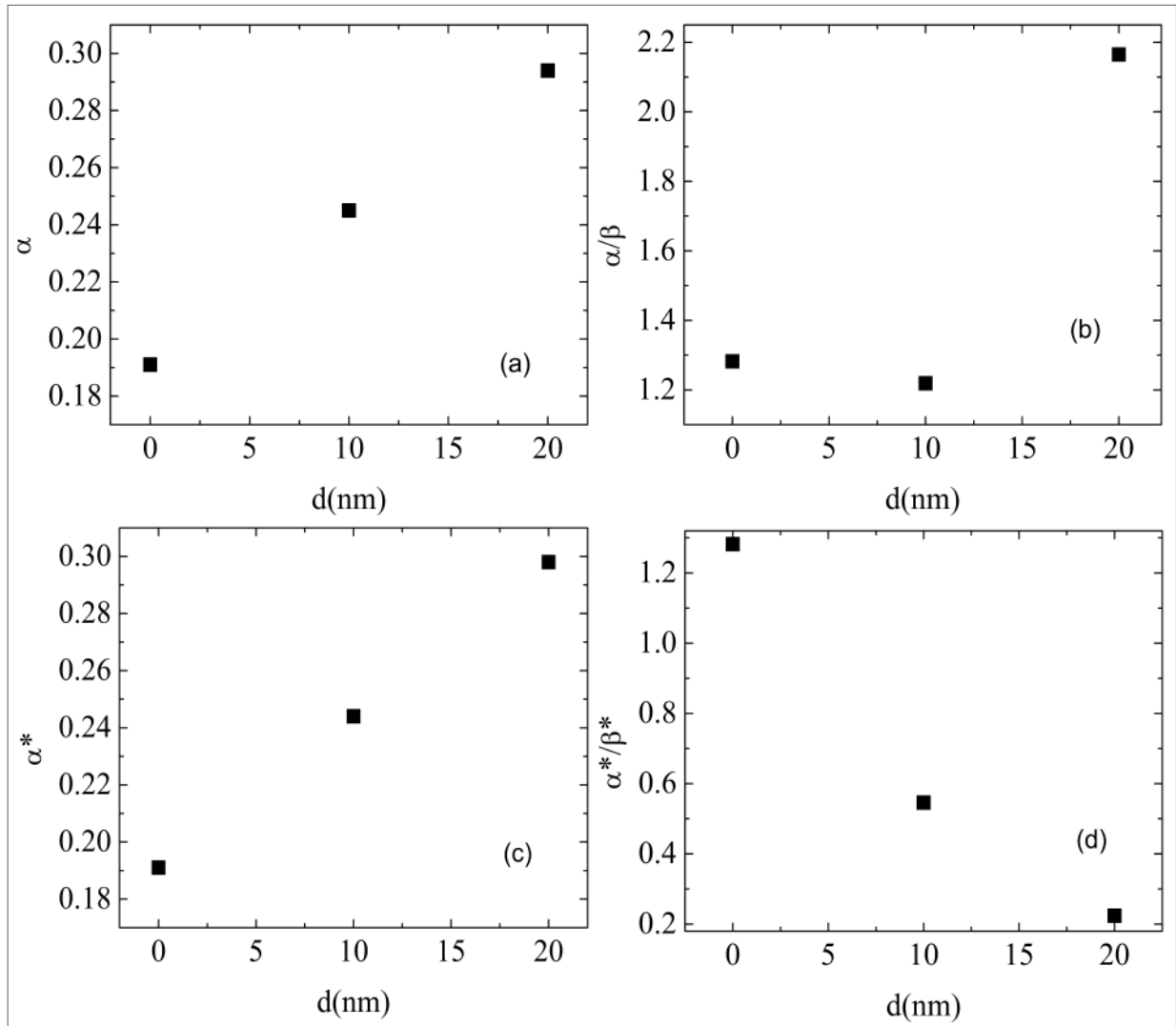
Figure 29 – Ni squared nanopillar shape anisotropy field versus packing factor $P^* = \frac{D^2-d^2}{a^2}$



Source: Elaborated by the author (2021)

has information on internal interactions in the pillars according to the proposed model and literature proposal (HERNÁNDEZ; REZENDE; AZEVEDO, 2008). The most representative is that these values, see Table 4, do not depend on how the packaging was chosen (P or P^*). These values can be used to estimate values of demagnetizing factor parallel to the nanopillar (HERNÁNDEZ; REZENDE; AZEVEDO, 2008).

Figure 30 – Ni squared nanopillar array coefficient adjustments for packing factor P and P^*



Source: Elaborated by the author (2021)

The values of $P_C = \frac{\alpha}{\beta}$ and $P_C^* = \frac{\alpha^*}{\beta^*}$ are important; P_C and P_C^* are the critical packing for which the disappearance of the anisotropy occurs, that is, $H_A = 0$. This critical value has been reported in several ways for nanowires, as it depends on how it is viewed as perfect cylinder, ellipsoid chain, etc (VÁZQUEZ et al., 2004). In the case of nanopillars, there is no difference and everything starts with the way the packing is seen. In a critical look at the curves in Figures 30b) and 30d) it can be seen totally different behaviors as the value of d changes. On

the other hand, the P_C value for $\frac{\alpha}{\beta}$ is noteworthy, as it is greater than 1. The choice of this parameter is even worse for $d = 20$ nm, because assuming it the system does not consider the cavity, approaching this result to that of an isotropic thin film. Therefore, it is not possible to calculate the anisotropy H_A in this case. Analysing the perpendicular results, it was observed divergences in the results of H_A analysing with Equations 4.2 and 4.3 which leads us to the idea that the perpendicular field model in square nanowire arrays still needs adjustments to its proposal. This could be associated with the aspect ratio of the length L of the pillars and $3D$, which would be the extension of the arrangement for $P = 1$ (HERNÁNDEZ; REZENDE; AZEVEDO, 2008). Even thus, it is striking and everything suggests that the most appropriate way to choose the packing in hollow columns is represented by P^* .

5 CONCLUSION

After analyzing the studies with FMR in singular nanopillar and nanopillar array it follows:

Isolated nanopillar:

1. The dipole effects due to the interaction between the internal and external faces are reverted in the increase of the predominant uniaxial anisotropy field.
2. Analysing the singular nanopillar primary peak results, it is found uniaxial anisotropy in the first order and comes from the longitudinal edges.
3. Uniaxial anisotropy in a perpendicular field leads to larger divergences for all values of d due to higher symmetry in the principal axis.
4. The value of shape anisotropy field H_A gets better as d increases for primary and secondary peaks for parallel and perpendicular fields.
5. Graphical analysis shows that primary peaks have more precise values than the secondary peaks, because the last can not be clearly identified as d decreases.

Nanopillar Array:

1. It can be seen an increase in anisotropy as the size of the hollow cavity increases inside the column and it is still possible to verify the reduction of this phenomenon as the distance between the columns in the arrangement decreases.
2. The perpendicular Kittel's equations for FMR were not useful to characterize the results to analyze the results for shape anisotropy field H_A .
3. In parallel analysis it was found that β^* and α^* grow up as the cavity size increases, here these phenomenological constants are obtained from the adjustment of H_A varying with packing factor considering the cavity of each nanopillar inside the array.
4. The results for H_A decreases as the packing factor increases, as expected by literature, because with great packing factors the geometry loses anisotropy.
5. Graphical analysis shows that $\frac{D^2-d^2}{a^2}$ presents better description for H_A analysing the results for $\frac{\alpha}{\beta}$ against $\frac{\alpha^*}{\beta^*}$.

6 OUTLOOK

The work presented is the beginning of new activities that will be done by the magnetic measurements research group. The next steps to upgrade the work presented here will be:

1. Map the FMR signal to analyze signal locations and verify that magnetic resonant signal comes from the side edges for singular nanopillars and nanopillar array.
2. Propose a model to adjust the shape anisotropy field H_A when the geometry is affected by the perpendicular field.
3. Use micromagnetic simulation results to simulate Magnetic Force Microscopy (MFM) images and improve understanding of different reversal modes compared to real images.
4. By using lithography, build similar structures and compare the results with which was obtained.
5. Study other cubic structures by using FMR simulations and to find a better model of packing factor.

REFERENCES

- ABO, G. S.; HONG, Y.-K.; PARK, J.; LEE, J.; LEE, W.; CHOI, B.-C. Definition of magnetic exchange length. *IEEE Transactions on Magnetics*, IEEE, v. 49, n. 8, p. 4937–4939, 2013.
- APPELL, D. Nanotechnology: Wired for success. *Nature*, Nature Publishing Group, v. 419, n. 6907, p. 553–556, 2002.
- ARFKEN, G. B.; WEBER, H. J. *Mathematical methods for physicists*. [S.l.]: American Association of Physics Teachers, 1999.
- BAKER, A.; BEG, M.; ASHTON, G.; ALBERT, M.; CHERNYSHENKO, D.; WANG, W.; ZHANG, S.; BISOTTI, M.-A.; FRANCHIN, M.; HU, C. L. et al. Proposal of a micromagnetic standard problem for ferromagnetic resonance simulations. *Journal of Magnetism and Magnetic Materials*, Elsevier, v. 421, p. 428–439, 2017.
- BALL, P. Roll up for the revolution. *Nature*, Nature Publishing Group, v. 414, n. 6860, p. 142–145, 2001.
- BERTOTTI, G. *Hysteresis in magnetism: for physicists, materials scientists, and engineers*. [S.l.]: Gulf Professional Publishing, 1998.
- BOARDMAN, R. P. *Computer simulation studies of magnetic nanostructures*. Tese (Doutorado) — University of Southampton, 2005.
- CHEN, D.-X.; BRUG, J. A.; GOLDFARB, R. B. Demagnetizing factors for cylinders. *IEEE Transactions on magnetics*, IEEE, v. 27, n. 4, p. 3601–3619, 1991.
- CULLITY, B. D.; GRAHAM, C. D. *Introduction to magnetic materials*. [S.l.]: John Wiley & Sons, 2011.
- CURIALE, J.; SÁNCHEZ, R. D.; RAMOS, C. A.; LEYVA, A.; BUTERA, A. Dynamic response of magnetic nanoparticles arranged in a tubular shape. *Journal of Magnetism and Magnetic Materials*, Elsevier, v. 320, n. 14, p. e218–e221, 2008.
- DAI, H.; HAFNER, J. H.; RINZLER, A. G.; COLBERT, D. T.; SMALLEY, R. E. Nanotubes as nanoprobe in scanning probe microscopy. *Nature*, Nature Publishing Group, v. 384, n. 6605, p. 147–150, 1996.
- DAO, N.; DONAHUE, M.; DUMITRU, I.; SPINU, L.; WHITTENBURG, S.; LODDER, J. Dynamic susceptibility of nanopillars. *Nanotechnology*, IOP Publishing, v. 15, n. 10, p. S634, 2004.
- DÁVILA, Y. G. Estados magnéticos e reversão da magnetização em nanoesferas ocas de cobalto. Universidade Federal de Pernambuco, 2019.
- DEMAND, M.; ENCINAS-OROPESA, A.; KENANE, S.; EBELS, U.; HUYNEN, I.; PIRAUX, L. Ferromagnetic resonance studies of nickel and permalloy nanowire arrays. *Journal of magnetism and magnetic materials*, Elsevier, v. 249, n. 1-2, p. 228–233, 2002.
- DERYCKE, V.; MARTEL, R.; APPENZELLER, J.; AVOURIS, P. Carbon nanotube inter-and intramolecular logic gates. *Nano letters*, ACS Publications, v. 1, n. 9, p. 453–456, 2001.

DONAHUE, M. J.; DONAHUE, M. *OOMMF user's guide, version 1.0*. [S.l.]: US Department of Commerce, National Institute of Standards and Technology, 1999.

D'AQUINO, M.; SERPICO, C.; MIANO, G.; FORESTIERE, C. A novel formulation for the numerical computation of magnetization modes in complex micromagnetic systems. *Journal of Computational Physics*, Elsevier, v. 228, n. 17, p. 6130–6149, 2009.

EAGLETON, T. S.; SEARSON, P. C. Electrochemical synthesis of 3d ordered ferromagnetic nickel replicas using self-assembled colloidal crystal templates. *Chemistry of materials*, ACS Publications, v. 16, n. 24, p. 5027–5032, 2004.

ENCINAS-OROPESA, A.; DEMAND, M.; PIRAUX, L.; HUYNEN, I.; EBELS, U. Dipolar interactions in arrays of nickel nanowires studied by ferromagnetic resonance. *Physical Review B*, APS, v. 63, n. 10, p. 104415, 2001.

ESCRIG, J.; LANDEROS, P.; ALTBIR, D.; VOGEL, E.; VARGAS, P. Phase diagrams of magnetic nanotubes. *Journal of magnetism and magnetic materials*, Elsevier, v. 308, n. 2, p. 233–237, 2007.

ESCRIG, J.; LAVIN, R.; PALMA, J.; DENARDIN, J.; ALTBIR, D.; CORTES, A.; GOMEZ, H. Geometry dependence of coercivity in ni nanowire arrays. *Nanotechnology*, IOP Publishing, v. 19, n. 7, p. 075713, 2008.

FISCHBACHER, T.; FRANCHIN, M.; BORDIGNON, G.; FANGOHR, H. A systematic approach to multiphysics extensions of finite-element-based micromagnetic simulations: Nmag. *IEEE Transactions on Magnetics*, v. 43, n. 6, p. 2896–2898, 2007.

FREI, E. H.; SHTRIKMAN, S.; TREVES, D. Critical size and nucleation field of ideal ferromagnetic particles. *Physical Review*, APS, v. 106, n. 3, p. 446, 1957.

FUENTES, G.; HOLANDA, J.; GUERRA, Y.; SILVA, D.; FARIAS, B.; PADRÓN-HERNÁNDEZ, E. Micromagnetic simulation and the angular dependence of coercivity and remanence for array of polycrystalline nickel nanowires. *Journal of Magnetism and Magnetic Materials*, Elsevier, v. 423, p. 262–266, 2017.

GILBERT, T. L. A phenomenological theory of damping in ferromagnetic materials. *IEEE transactions on magnetics*, IEEE, v. 40, n. 6, p. 3443–3449, 2004.

GUBIN, S. P. *Magnetic nanoparticles*. [S.l.]: John Wiley & Sons, 2009.

GUERRA, Y.; SILVA, J. da; VIANA, B. C.; PADRÓN-HERNÁNDEZ, E. Dipolar magnetic interactions in 3×3 arrays of rectangular ni nanopillars. *Physica E: Low-dimensional Systems and Nanostructures*, Elsevier, v. 126, p. 114439, 2021.

GUIMARÃES, A. P.; OLIVEIRA, I. S. *Magnetism and magnetic resonance in solids*. [S.l.]: Wiley New York, 1998.

GUSEV, A. I.; REMPEL, A. A. *Nanocrystalline materials*. [S.l.]: Cambridge Int Science Publishing, 2004.

HAN, G.; ZONG, B.; LUO, P.; WU, Y. Angular dependence of the coercivity and remanence of ferromagnetic nanowire arrays. *Journal of Applied Physics*, American Institute of Physics, v. 93, n. 11, p. 9202–9207, 2003.

- HERNÁNDEZ, E. P. Características microestructuras e propriedades magnéticas de arranjos de nanofios magnéticos. Universidade Federal de Pernambuco, 2009.
- HERNÁNDEZ, E. P.; REZENDE, S.; AZEVEDO, A. Effective field investigation in arrays of polycrystalline ferromagnetic nanowires. *Journal of Applied Physics*, American Institute of Physics, v. 103, n. 7, p. 07D506, 2008.
- HUANG, J.; QI, Z.; LI, L.; WANG, H.; XUE, S.; ZHANG, B.; ZHANG, X.; WANG, H. Self-assembled vertically aligned ni nanopillars in ceo 2 with anisotropic magnetic and transport properties for energy applications. *Nanoscale*, Royal Society of Chemistry, v. 10, n. 36, p. 17182–17188, 2018.
- HUSSAIN, B.; COTTAM, M. Effects of an external magnetic field on spin waves in finite-length ferromagnetic nanotubes. *Journal of Magnetism and Magnetic Materials*, Elsevier, v. 539, p. 168344, 2021.
- JAIMES, D. M. A.; RAVIOLO, S.; CARBALLO, J. M.; BAJALES, N.; ESCRIG, J. Wave reversion mode stability as a function of diameter and wall thickness for permalloy and nickel nanotubes. *Journal of Magnetism and Magnetic Materials*, Elsevier, v. 523, p. 167578, 2021.
- KAKAY, A.; WESTPHAL, E.; HERTEL, R. Speedup of fem micromagnetic simulations with graphical processing units. *IEEE transactions on magnetics*, IEEE, v. 46, n. 6, p. 2303–2306, 2010.
- KARDAR, M. *Statistical physics of particles*. [S.l.]: Cambridge University Press, 2007.
- KIM, P.; LIEBER, C. M. Nanotube nanotweezers. *Science*, American Association for the Advancement of Science, v. 286, n. 5447, p. 2148–2150, 1999.
- KITTEL, C. Interpretation of anomalous larmor frequencies in ferromagnetic resonance experiment. *Physical Review*, APS, v. 71, n. 4, p. 270, 1947.
- KOOLS, F.; MOREL, A. Ferrite magnets: Improved performance. In: BUSCHOW, K. J.; CAHN, R. W.; FLEMINGS, M. C.; ILSCHNER, B.; KRAMER, E. J.; MAHAJAN, S.; VEYSSIERE, P. (Ed.). *Encyclopedia of Materials: Science and Technology*. Oxford: Elsevier, 2004. p. 1–5. ISBN 978-0-08-043152-9. Disponível em: <<https://www.sciencedirect.com/science/article/pii/B0080431526019082>>.
- KRAUS, L.; INFANTE, G.; FRAIT, Z.; VÁZQUEZ, M. Ferromagnetic resonance in microwires and nanowires. *Physical Review B*, APS, v. 83, n. 17, p. 174438, 2011.
- KRONMÜLLER, H.; PARKIN, S. Handbook of magnetism and advanced magnetic materials. John Wiley & Sons Ltd., 2007.
- LANDAU, L.; LIFSHITZ, E. On the theory of the dispersion of magnetic permeability in ferromagnetic bodies. In: *Perspectives in Theoretical Physics*. [S.l.]: Elsevier, 1992. p. 51–65.
- LANDEROS, P. A.; ESCRIG, S.; SALCEDO, J. E. and albir, d. *Appl. Phys. Lett*, v. 90, p. 102501, 2007.
- LENZ, K.; NARKOWICZ, R.; WAGNER, K.; REICHE, C. F.; KÖRNER, J.; SCHNEIDER, T.; KÁKAY, A.; SCHULTHEISS, H.; WEISSKER, U.; WOLF, D. et al. Magnetization dynamics of an individual single-crystalline fe-filled carbon nanotube. *Small*, Wiley Online Library, v. 15, n. 49, p. 1904315, 2019.

- MAHALINGAM, S. S.; MANIKANDAN, B.; AROCKIARAJ, S. Review–micromagnetic simulation using oommf and experimental investigations on nano composite magnets. In: IOP PUBLISHING. *Journal of Physics: Conference Series*. [S.l.], 2019. v. 1172, n. 1, p. 012070.
- MCMICHAEL, R. D.; STILES, M. D. Magnetic normal modes of nanoelements. *Journal of Applied Physics*, American Institute of Physics, v. 97, n. 10, p. 10J901, 2005.
- MOORE, S. A better way to measure progress in semiconductors. *The node is nonsense*, "IEEE Spectrum", 2020.
- MORIARTY, P. Nanostructured materials. *Reports on Progress in Physics*, IOP Publishing, v. 64, n. 3, p. 297, 2001.
- NEUDECKER, I.; WOLTERSDORF, G.; HEINRICH, B.; OKUNO, T.; GUBBIOTTI, G.; BACK, C. H. Comparison of frequency, field, and time domain ferromagnetic resonance methods. *Journal of Magnetism and Magnetic Materials*, Elsevier, v. 307, n. 1, p. 148–156, 2006.
- OTÁLORA, J. A.; YAN, M.; SCHULTHEISS, H.; HERTEL, R.; KÁKAY, A. Asymmetric spin-wave dispersion in ferromagnetic nanotubes induced by surface curvature. *Physical Review B*, APS, v. 95, n. 18, p. 184415, 2017.
- OUSTERHOUT, J.; JONES, J. *Tcl and the Tk Toolkit*. [S.l.]: Addison-Wesley Professional, 2009.
- PIRAUX, L. Magnetic nanowires. *Applied Sciences*, Multidisciplinary Digital Publishing Institute, v. 10, n. 5, p. 1832, 2020.
- QUALCOMM. *Qualcomm Snapdragon 888 5G Mobile Platform: Latest 5G Snapdragon Processor*. Qualcomm, 2021. Disponível em: <<https://www.qualcomm.com/products/snapdragon-888-5g-mobile-platform>>.
- RAPOSO, V.; ZAZO, M.; FLORES, A.; GARCIA, J.; VEGA, V.; IÑIGUEZ, J.; PRIDA, V. Ferromagnetic resonance in low interacting permalloy nanowire arrays. *Journal of Applied Physics*, AIP Publishing LLC, v. 119, n. 14, p. 143903, 2016.
- REICH, D.; TANASE, M.; HULTGREN, A.; BAUER, L.; CHEN, C.; MEYER, G. Biological applications of multifunctional magnetic nanowires. *Journal of Applied Physics*, American Institute of Physics, v. 93, n. 10, p. 7275–7280, 2003.
- REZENDE, S. M. *Fundamentals of Magnonics*. [S.l.]: Springer, 2020. v. 969.
- RUDI, K.; LARSEN, F.; JAKOBSEN, K. S. Detection of toxin-producing cyanobacteria by use of paramagnetic beads for cell concentration and dna purification. *Applied and Environmental Microbiology*, Am Soc Microbiol, v. 64, n. 1, p. 34–37, 1998.
- RUECKES, T.; KIM, K.; JOSELEVICH, E.; TSENG, G. Y.; CHEUNG, C.-L.; LIEBER, C. M. Carbon nanotube-based nonvolatile random access memory for molecular computing. *science*, American Association for the Advancement of Science, v. 289, n. 5476, p. 94–97, 2000.
- SAAVEDRA, E.; SAEZ, G.; DÍAZ, P.; CISTERNAS, E.; VOGEL, E. E.; ESCRIG, J. Dynamic susceptibility of modulated magnetic nanowires. *AIP Advances*, AIP Publishing LLC, v. 9, n. 6, p. 065007, 2019.

- SAKURAI, J. J.; COMMIN, E. D. *Modern quantum mechanics, revised edition*. [S.l.]: American Association of Physics Teachers, 1995.
- SALINAS, H.; RESTREPO, J.; IGLESIAS, Ò. Tailoring dual reversal modes by helicity control in ferromagnetic nanotubes. *Physical Review B*, APS, v. 101, n. 5, p. 054419, 2020.
- SHARMA, M.; BASU, A.; KUARN, B. K. Magnetization reversal switching in nanocylinders using dynamic techniques. *Journal of Magnetism and Magnetic Materials*, Elsevier, v. 476, p. 234–242, 2019.
- SILVA, J. da; GUERRA, Y.; PADRÓN-HERNÁNDEZ, E. Simulations of fmr for study the shape anisotropy in square hollow nanopillars. *Journal of Magnetism and Magnetic Materials*, Elsevier, p. 168642, 2021.
- STONER, E. C.; WOHLFARTH, E. A mechanism of magnetic hysteresis in heterogeneous alloys. *Philosophical Transactions of the Royal Society of London. Series A, Mathematical and Physical Sciences*, The Royal Society London, v. 240, n. 826, p. 599–642, 1948.
- STROUSTRUP, B. *The C++ programming language*. [S.l.]: Pearson Education India, 2000.
- TEHRANI, M. D.; KIM, M. O.; YOON, J. A novel electromagnetic actuation system for magnetic nanoparticle guidance in blood vessels. *IEEE transactions on magnetics*, IEEE, v. 50, n. 7, p. 1–12, 2014.
- VÁZQUEZ, M.; HERNÁNDEZ-VÉLEZ, M.; PIROTA, K.; ASENJO, A.; NAVAS, D.; VELÁZQUEZ, J.; VARGAS, P.; RAMOS, C. Arrays of ni nanowires in alumina membranes: magnetic properties and spatial ordering. *The European Physical Journal B-Condensed Matter and Complex Systems*, Springer, v. 40, n. 4, p. 489–497, 2004.
- WAGNER, K.; KÖRBER, L.; STIENEN, S.; LINDNER, J.; FARLE, M.; KÁKAY, A. Numerical ferromagnetic resonance experiments in nanosized elements. *IEEE Magnetics Letters*, IEEE, v. 12, p. 1–5, 2021.
- YALÇIN, O. *Ferromagnetic Resonance: Theory and Applications*. [S.l.]: BoD–Books on Demand, 2013.
- YALÇIN, O.; YILDIZ, F.; ÖZDEMİR, M.; AKTAŞ, B.; KÖSEOĞLU, Y.; BAL, M.; TUOMINEN, M. Ferromagnetic resonance studies of co nanowire arrays. *Journal of magnetism and magnetic materials*, Elsevier, v. 272, p. 1684–1685, 2004.
- YANG, H.; LI, Y.; ZENG, M.; CAO, W.; BAILEY, W. E.; YU, R. Static and dynamic magnetization of gradient feni alloy nanowire. *Scientific reports*, Nature Publishing Group, v. 6, n. 1, p. 1–9, 2016.
- ZÉLIS, P. M.; VEGA, V.; PRIDA, V.; COSTA-ARZUZA, L. C.; BERON, F.; PIROTA, K. R.; LÓPEZ-RUIZ, R.; SÁNCHEZ, F. H. Effective demagnetizing tensors in arrays of magnetic nanopillars. *Physical Review B*, APS, v. 96, n. 17, p. 174427, 2017.
- ZHANG, H.; DIVAN, R.; WANG, P. Ferromagnetic resonance of a single magnetic nanowire measured with an on-chip microwave interferometer. *Review of scientific instruments*, American Institute of Physics, v. 82, n. 5, p. 054704, 2011.
- ZHANG, X.; LI, W.; IRFAN, M.; PARAJULI, S.; WEI, J.; YAN, Z.; WANG, X.; AHMAD, N.; FENG, J.; YU, G. et al. Fabrication and characterization of yig nanotubes. *Journal of Magnetism and Magnetic Materials*, Elsevier, v. 482, p. 358–363, 2019.

ANNEX A – PAPERS RESULTING FROM THIS WORK

- **SILVA, J. da**; GUERRA, Y.; PADRÓN-HERNÁNDEZ, E. Simulations of fmr for study the shape anisotropy in square hollow nanopillars. *Journal of Magnetism and Magnetic Materials*, Elsevier, p. 168642, 2021. Doi: 10.1016/j.jmmm.2021.168642
- GUERRA, Y.; **SILVA, J. da**; VIANA, B. C.; PADRÓN-HERNÁNDEZ, E. Dipolar magnetic interactions in 3×3 arrays of rectangular ni nanopillars. *Physica E: Low-dimensional Systems and Nanostructures*, Elsevier, v. 126, p. 114439, 2021. Doi: 10.1016/j.physe.2020.114439
- **J.F.O. da Silva**, E. Padrón-Hernández. Magnetic anisotropy investigation by FMR in a 3×3 array of square hollow Ni nanopillars (Submitted).